Geophysical Journal International

Geophys. J. Int. (2014) **199,** 480–498
GJI Geodynamics and tectonics

doi: 10.1093/gji/ggu225

Shear velocity model for the Kyrgyz Tien Shan from joint inversion of receiver function and surface wave data

Amy Gilligan,[1] Steven W. Roecker,[2] Keith F. Priestley[1] and Ceri Nunn[1]

[1]*Bullard Laboratories, Department of Earth Sciences, University of Cambridge, UK. E-mail: arg54@cam.ac.uk*
[2]*Department of Earth and Environmental Sciences, Rensselaer Polytechnic Institute, Troy, NY, USA*

Accepted 2014 June 11. Received 2014 June 10; in original form 2014 February 13

SUMMARY

The Tien Shan is the largest active intracontinental orogenic belt on Earth. To better understand the processes causing mountains to form at great distances from a plate boundary, we analyse passive source seismic data collected on 40 broad-band stations of the MANAS project (2005–2007) and 12 stations of the permanent KRNET seismic network to determine variations in crustal thickness and shear wave speed across the range. We jointly invert *P*- and *S*-wave receiver functions with surface wave observations from both earthquakes and ambient noise to reduce the ambiguity inherent in the images obtained from the techniques applied individually. Inclusion of ambient noise data improves constraints on the upper crust by allowing dispersion measurements to be made at shorter periods. Joint inversion can also reduce the ambiguity in interpretation by revealing the extent to which various features in the receiver functions are amplified or eliminated by interference from multiples. The resulting wave speed model shows a variation in crustal thickness across the range. We find that crustal velocities extend to ∼75 km beneath the Kokshaal Range, which we attribute to underthrusting of the Tarim Basin beneath the southern Tien Shan. This result supports the plate model of intracontinental convergence. Crustal thickness elsewhere beneath the range is about 50 km, including beneath the Naryn Valley in the central Tien Shan where previous studies reported a shallow Moho. This difference apparently is the result of wave speed variations in the upper crust that were not previously taken into account. Finally, a high velocity lid appears in the upper mantle of the Central and Northern part of the Tien Shan, which we interpret as a remnant of material that may have delaminated elsewhere under the range.

Key words: Tomography; Surface waves and free oscillations; Intra-plate processes; Continental tectonics: compressional; Crustal structure; Asia.

1 INTRODUCTION

The Tien Shan, situated some 1000–3000 km north of the collisional front between Eurasia and India, forms the largest active intracontinental orogenic belt on Earth. The belt is seismically active (e.g. Ni 1978; Tapponnier & Molnar 1979; Molnar & Ghose 2000; Sloan *et al.* 2011) and the highest peaks exceed 7000 m. The intracontinental setting of the Tien Shan is unusual but analogous to that of other mountain ranges such as the Atlas Mountains (Beauchamp *et al.* 1996) and Laramides (English & Johnston 2004). Hence, illuminating the dynamics of the Tien Shan can aid our understanding of the processes involved in previous episodes of intracontinental mountain building.

The collision between India and Eurasia began around 50–55 Ma (Molnar & Tapponnier 1975; Searle *et al.* 1987). Thermochronologic and stratigraphic studies from the southern and eastern Tien Shan suggest that current deformation in the range began 24–20 Ma (Sobel & Dumitru 1997; Yin *et al.* 1998), while geodetic studies (Avouac *et al.* 1993; Abdrakhmatov *et al.* 1996) and thermochronologic studies from the northern Tien Shan (Bullen *et al.* 2003) suggest that deformation initiated more recently, perhaps around 10 Ma. GPS measurements indicate that about 20 mm yr^{-1} of north–south shortening, or approximately 40 per cent of the total convergence between India and Eurasia, is being accommodated in the Tien Shan (Abdrakhmatov *et al.* 1996; Reigber *et al.* 2001; Wang *et al.* 2001; Zubovich *et al.* 2010), of which 12–13 mm yr^{-1} occurs within the Kyrgz Tien Shan (Abdrakhmatov *et al.* 1996). Deformation is distributed along folds and dip-slip faults across the whole range (Thompson *et al.* 2002), resulting in a basin and range type topography.

A fundamental question posed by the Tien Shan is why intracontinental orogenic belts exist at all. One hypothesis is that mountains form in the middle of continents due to forces applied remotely, with the location of the deformation determined by weaknesses in

the lithosphere that arise due to temperature or chemical differences (Roecker *et al.* 1993). It is conceptually straight forward to relate formation of the Tien Shan to the collision between India and Eurasia; shortening occurs due to the transfer of stress from the collision front via the Tarim basin (Molnar & Tapponnier 1975). This may have reactivated some features, such as thrust faults, from the collisional events in the Palaeozoic that occurred in the region where we now find the Tien Shan (Thompson *et al.* 2002), but a question remains as to why some of these features were activated while others were ignored. An alternative explanation invokes processes such as small-scale convection in the mantle occurring locally beneath regions where the mountains form as key to shortening and mountain formation (Thompson *et al.* 2002).

Results from some prior investigations in this region support the hypothesis that the upper mantle beneath the Tien Shan is weak, and hence a candidate for concentration of strain from the ongoing collision. For example, upper mantle compressional wave speeds tend to be slow (Vinnik & Saipbekova 1984; Roecker *et al.* 1993) and anisotropy from shear wave splitting (Makeyeva *et al.* 1992) reveals strain in the upper mantle parallel to the direction of maximum compression. Chen *et al.* (1997) used *P*s conversions to suggest the that 410 km discontinuity beneath the central Tien Shan is elevated. Further, a *P*-wave tomography model from Li *et al.* (2009) suggests that this part of the lithosphere was removed by syphoning into thickened roots beneath both the Kyrgyz and Kokshaal ranges. An implication from all of these studies is that the lithosphere beneath much of the Krygyz Tien Shan has been removed, or at least severely attenuated.

At the same time, other investigations, in particular the receiver function studies of Oreshin *et al.* (2002) and Vinnik *et al.* (2004, 2006), reveal the presence of a thin lithospheric lid with high elastic wave speeds and suggest that this lid could be strong enough to allow stress transfer from the Tarim basin north to the Kazakh Shield. The presence of a strong lithospheric lid in the upper mantle is supported as well by estimates of variations in crustal thickness of 35–70 km across the range (Krestnikov *et al.* 1982; Roecker 2001; Oreshin *et al.* 2002; Vinnik *et al.* 2004, 2006; Makarov *et al.* 2010). The thinnest crust, beneath the Naryn Valley in the middle of the Tien Shan, could be interpreted as the lid inhibiting significant shortening in the interior of the range.

Another first order question concerns the nature of convergence of the crust and upper mantle in intracontinental settings. End-member scenarios are the plate model, where most of the convergence is taken up along a discrete boundary, and the 'accordion' model, where shortening is accommodated more or less continuously across a broad region. Estimates of the amount of shortening from reconstructions (Thompson *et al.* 2002) and from the depth to the present-day Moho (Roecker 2001) are on the order of 80 km. Given a shortening rate of 22 mm yr^{-1}, this could mean that there was no significant convergence in this part of central Asia until recently, or that most of the convergence was taken up by, for example, subduction of the Tarim Basin and/or Chu Basin along the edges of the Tien Shan. The former scenario would corroborate the accordion model interpretation, the latter the plate boundary interpretation.

In support of the plate boundary interpretation, Makarov *et al.* (2010) find thick crust beneath the southern Tien Shan and claim to resolve a coherent structural interface between the Tarim Basin and the Tien Shan proper from the surface to at least the Moho. They interpret their results as evidence of underthrusting of the Tarim Basin beneath the Tien Shan. Vinnik *et al.* (2006) also found thick crust beneath the southern Tien Shan using *P* and *S* receiver functions. A thickened crust is supported as well by other studies in the region (e.g. Poupinet *et al.* 2002). The *P*-wave tomography results of Li *et al.* (2009) could be interpreted as evidence for subducted lithosphere from both north and south of the Tien Shan, implying a long history of plate-like convergence preceding the current deformation regime in the Tien Shan. At the same time, one could argue that these high wave speed features are a consequence of localized lithospheric shortening, and hence could have been generated without consumption of the Tarim crust. Geodetic results (e.g. Thompson *et al.* 2002) suggest that crustal shortening, while in some sense distributed across the Tien Shan, is concentrated along only four or five distinct zones. While intriguing, these observations do not tell us much about the deformation regime in the lower crust and upper mantle.

These issues can be better illuminated by higher resolution images of elastic wave speeds in the crust and upper mantle beneath the Tien Shan. For example, low velocities persisting at depth may indicate thickened or subducted crust, and high velocities in the upper mantle may suggest the presence of a lithospheric lid. These could allow us to discern the different mechanisms through which convergence is occurring. In this study, we attempt to generate such images by jointly inverting fundamental mode Raleigh wave group velocity dispersion curves from both ambient noise and earthquake sources, and *P* and *S* receiver functions. These data are derived from seismograms recorded by a dense linear array of broad-band seismic stations deployed in in the Kyrgyz (central) Tien Shan (Fig. 1).

We combine surface waves from earthquakes with those from ambient noise measurements to broaden the band over which we estimate group velocities, primarily to improve resolution at shallower (crustal) depths. Surface waves provide reasonable estimates of absolute wave speeds, but are relatively insensitive to first-order discontinuities, while receiver functions are sensitive to short wavelength changes in media properties but with a strong velocity–depth trade-off. Because the limitations are largely complimentary, one can expect that the ambiguities resulting from the analysis of one type of observation will be reduced when combined with the other, and joint inversion increases the likelihood that the resulting model will be compatible with both sets of observation.

2 DATA AND METHODOLOGY

Most of the seismic data analysed in this study were recorded by the passive source component of the MANAS (Middle AsiaN Active Source) project. An array of broad-band seismometers was deployed across the width of the Kyrgyz Tien Shan (Fig. 1b). The MANAS deployment consisted of five Guralp CMG-3ESPs and 35 Streckeisen STS-2s installed in a quasi-linear geometry with a spacing of about 10 km, and was operational from 2005 June to 2007 July. Each station recorded continuously at 100 sps with Quanterra Q330 acquisition systems. Because of data quality issues stemming from technical recording problems, seismograms from three of the MANAS stations (BRID, AHQI and QUAR) were not used in this analysis. The MANAS data were supplemented with seismograms from the KRNET permanent broad-band network located to the the northern side of the range (Fig. 1b). The KRNET stations used include nine CMG-3ESPs, two CMG-6TDs and one STS-2.

2.1 Receiver functions

In this study, we calculate both *P* and *S* receiver functions from the records of teleseismic earthquakes recorded by stations in the MANAS array. The methodology for computing *P* and

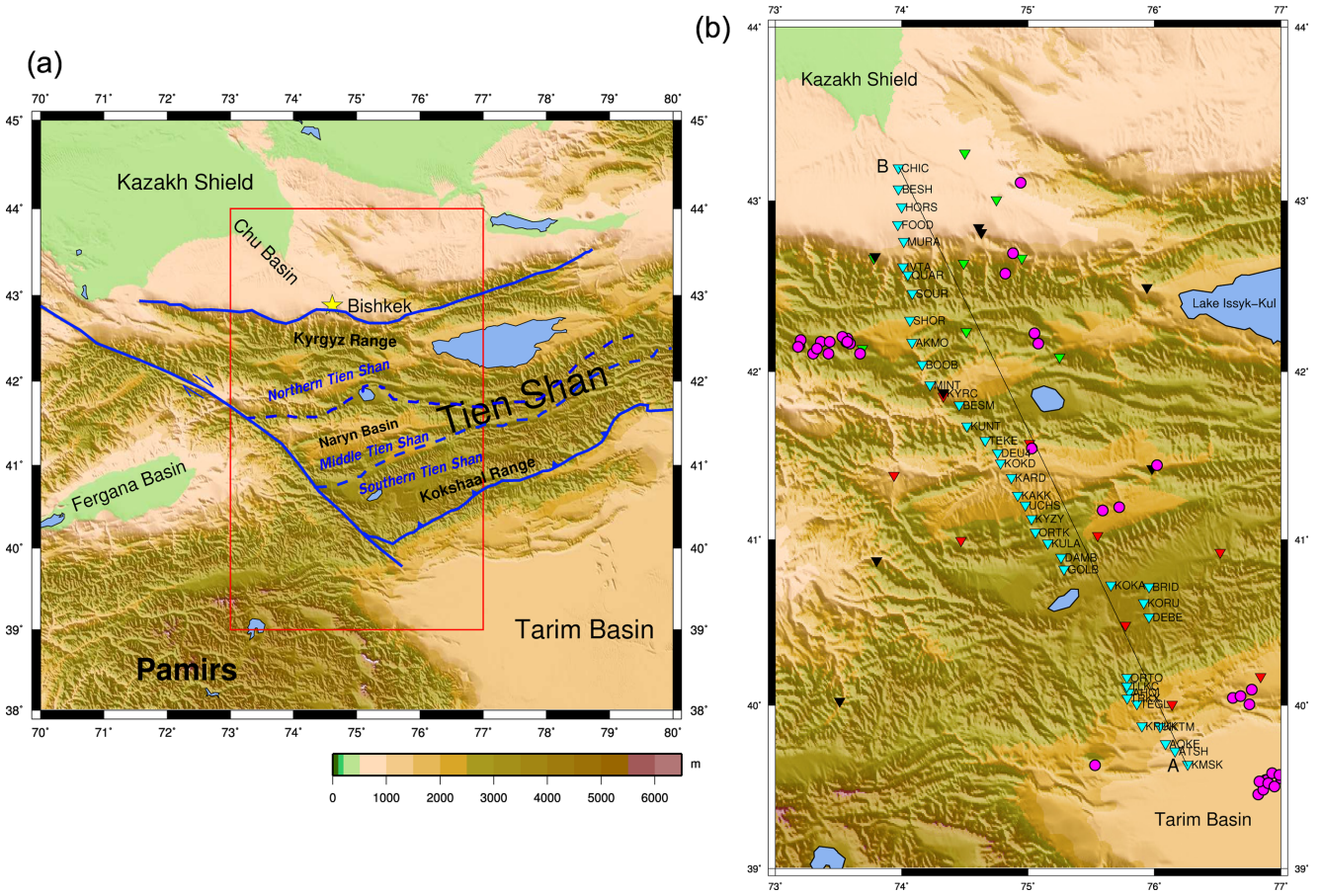

Figure 1. (a) Map of the area around the Kygyz Tien Shan. Dashed blue lines show the terrane boundaries between the Northern, Middle and Southern Tien Shan, and solid blue lines are faults (after Makarov *et al.* (2010)). Red rectangle highlight area in (b). (b) Triangles are stations: cyan MANAS, green KNET, black KRNET and red GHENGIS. Data from the MANAS stations are used to calculate the *P*-receiver functions and ambient noise Rayleigh-wave dispersion curves used in the inversions below. Receiver functions results from Bump & Sheehan (1998); Vinnik *et al.* (2004, 2006) are calculated at the KNET and GHENGIS stations. Magenta circles show the locations of earthquakes from Sloan *et al.* (2011). The line A–B shows the line of section.

S receiver functions is described in detail elsewhere (e.g. Vinnik 1977; Langston 1979; Farra & Vinnik 2000; Kind *et al.* 2012), and we give a brief outline here. In both cases the seismograms are first rotated into a reference frame based on the principal component of motion of the incident phase, in order to maximize the energy of the converted mode. Using the nomenclature of Farra & Vinnik (2000) and Vinnik (1977), for *P* receiver functions this is the (L, H, Q) frame, where L is longitudinal (P), Q is in perpendicular to L in the longitudinal-radial plane (SV) and H is transverse (SH). For *S* receiver functions this is the (M, L, O) frame, where M is the principal horizontal component of motion for the *S* arrival, L is longitudinal, and O is perpendicular to M and L. After rotation, the mode-converted component (Q or L) is deconvolved by the component of the principal phase (L or M) using iterative deconvolution (Ammon 1991) with a Gaussian pre-filter width of 1.67 s.

For both *P* and *S* receiver functions we select teleseismic events with $M > 6$ that occurred while the MANAS array was operational and for which the *P* or *S* arrival could be clearly identified. In all, 25 and 37 events were used to calculate *P* and *S* receiver functions, respectively (Fig. 2).

We stack the deconvolved receiver functions to increase the signal-to-noise ratio. When stacking individual receiver functions we make the assumption that the Earth is laterally homogeneous and isotropic in the vicinity of any particular point. For both *P* and *S* receiver functions we determined the location of the piercing point for a 50-km-thick crust derived using the IASPI91 model (Kennett & Engdahl 1991). Previous work (Oreshin *et al.* 2002; Vinnik *et al.* 2004, 2006; Makarov *et al.* 2010) suggests that the thickness of the crust varies between about 40 and 65 km, and so we chose 50 km as an appropriate average crustal thickness for this region. A profile along the azimuth of the deployment (line A–B in Fig. 1) was divided into 10 km segments and the receiver functions with piercing points falling in this bin were stacked (Fig. 3). Prior to stacking, the individual receiver functions in each bin were visually inspected for quality, and those that appeared anomalous were removed. A total of 572 individual *P* receiver functions and 972 individual *S* receiver functions were used in the stacks.

The *P* receiver functions were stacked using a straight summation. *S* receiver functions were stacked using a method similar to that described by Farra & Vinnik (2000) to mitigate effects of weak anisotropy.

2.2 Fundamental mode Rayleigh wave group velocities

We obtain fundamental mode Rayleigh wave group velocity dispersion curves from records of both earthquakes and ambient noise. The path averaged group velocity measurements are then used in a tomographic inversion to produce group velocity maps. These maps

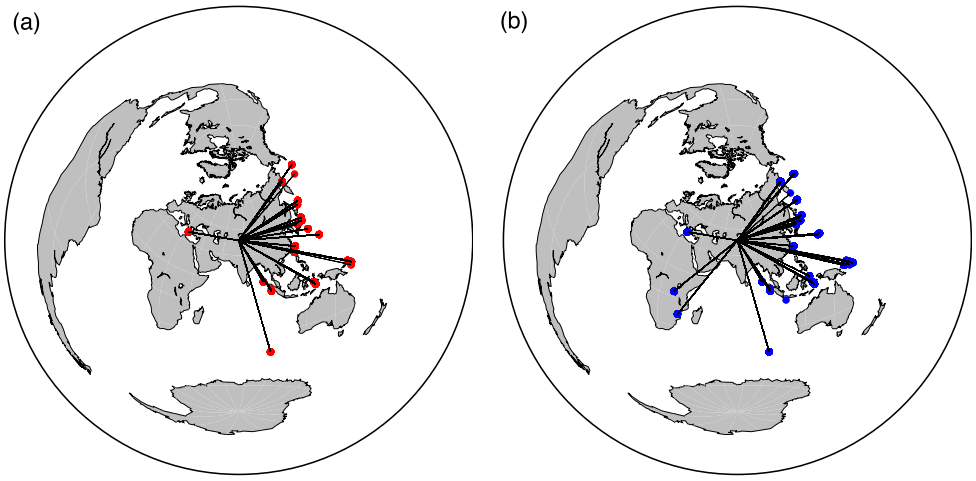

Figure 2. (a) Red circles mark the locations of earthquakes used to construct the *P* receiver functions. The majority of events used were in the Pacific or Sumatra, with a backazimuth range 36–165°. There is one event occurring in the Hellenic trench with a backazimuth of 282°. The events occur in an epicentral distance range 37–91°. (b) Blue circles mark the locations of earthquakes used to construct the *S* receiver functions. The majority of events used were in the Pacific or Sumatra. The events have a backazimuth range of 36–282°. The events occur in an epicentral distance range 37–91°.

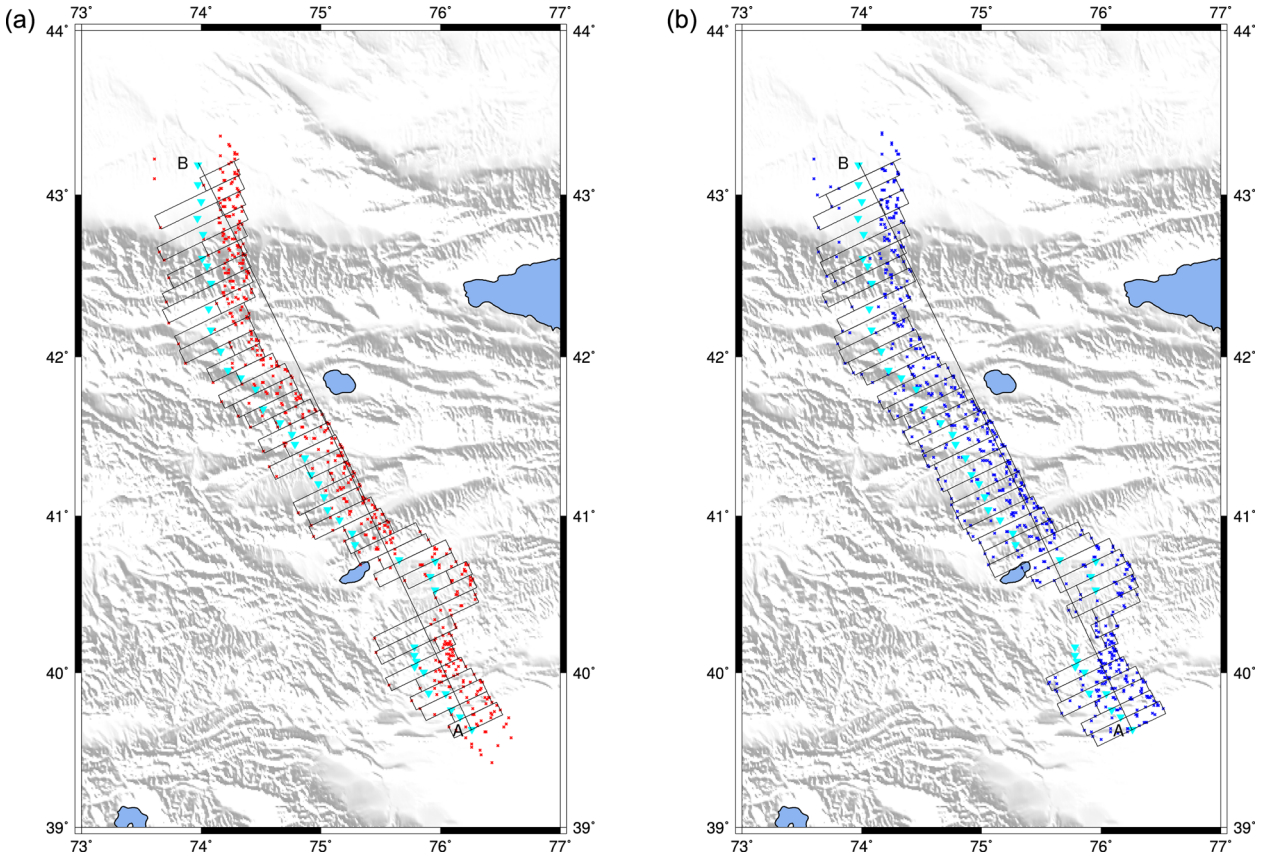

Figure 3. (a) PRF piercing points (red crosses) and bins used in stacking (b) SRF piercing points (blue crosses) and bins used in stacking.

then constitute the observations that we use to invert for shear wave velocities jointly with the receiver functions.

Green's functions from ambient noise data are particularly well suited for surface wave analysis (Shapiro & Campillo 2004). There are two principal advantages in using ambient noise data: first, it allows surface wave measurements to be made along paths that are not possible using just earthquake–station pairs, and, second, it is possible to obtain dispersion measurements at periods short enough to be sensitive to wave speeds in the upper crust.

In selecting earthquake surface wave data recorded by the MANAS and KRNET stations, we start with events with $M > 4.5$ located within 3000 km of the MANAS array. We assume a great circle propagation path and generate Rayleigh wave dispersion curves for 1751 paths between 217 events and 58 stations (Fig. 4). We also include Rayleigh wave measurements made by Nunn *et al.* (2014) for 1529 paths from 49 events, recorded at 94 stations, and measurements made by Acton *et al.* (2010) and Rham (2009) for 7277 paths from 2546 events at 662 stations.

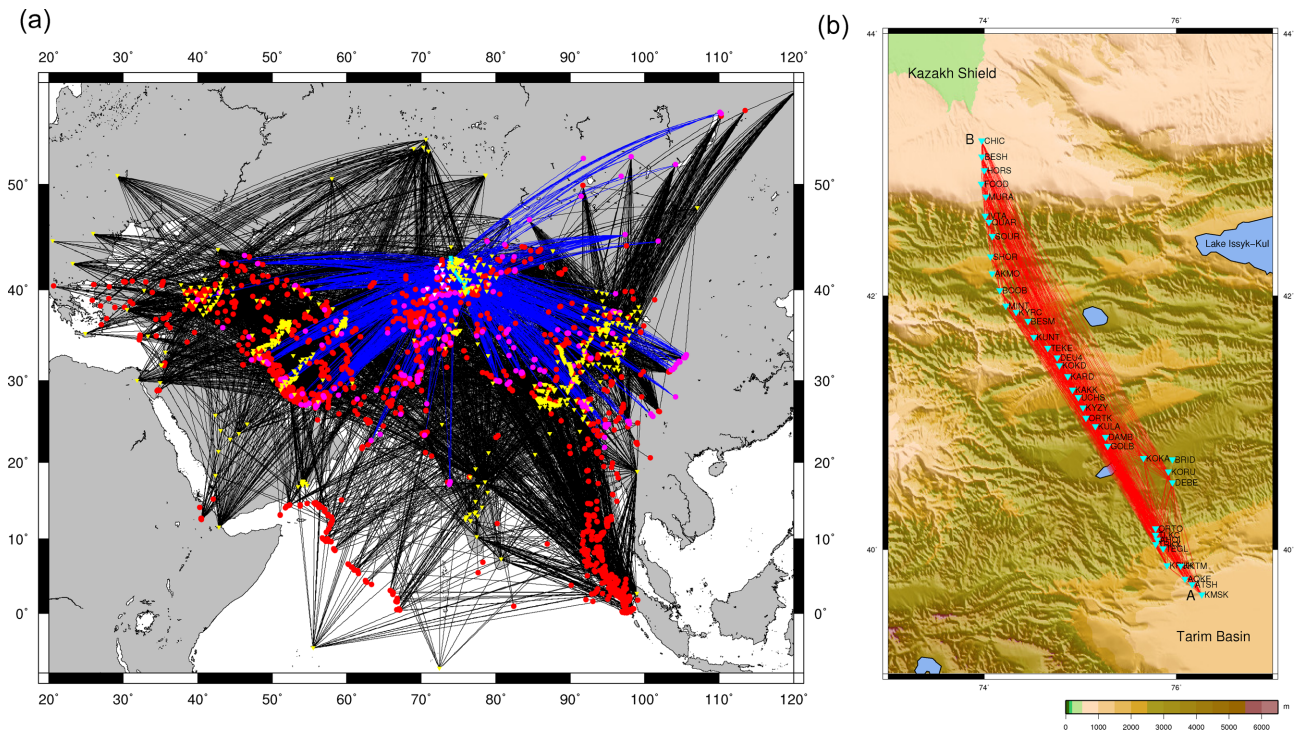

Figure 4. (a) Paths between stations and earthquakes used to generate path average Rayleigh wave dispersion curves. Blue lines are this study and black lines are from Nunn *et al.* (2014); Acton *et al.* (2010); Rham (2009). (b) Paths used to generate Rayleigh wave group velocity dispersion curves from the cross-correlations of ambient noise data between station pairs.

To obtain Rayleigh wave dispersion curves from ambient noise, we cross-correlate continuous recordings of the vertical component of motion between station pairs and follow the the method of Bensen *et al.* (2007) to calculate intrastation Green's functions. Seismograms are decimated to 1 sps, split into 1 d intervals, band-pass filtered from 0.01 to 0.2 Hz, spectrally whitened and normalized using a running mean normalization to remove signals from earthquakes. The time-series for each day and for each station pair are then cross-correlated, and the resultant cross-correlations for each station pair are stacked. A total of 666 cross-correlations were calculated and stacked over a period of 1.75 yr (Fig. 4).

The resulting Green's function estimate for each pair has a causal and an acausal part (Fig. 5). If the sources of noise are isotropically distributed, the estimated Green's function should be symmetric; the asymmetry in our estimates suggests that sources of noise, particularly in the 5–20 s band, are predominantly from the south. Given that the Arctic Ocean is covered with ice for portions of the year, it is not surprising that noise from the Indian Ocean dominates the noise wavefield. Following Bensen *et al.* (2007), we take an average of the causal and acausal sides of the cross-correlation as the Green's function.

2.2.1 *Group velocity determination*

We calculate group velocity dispersion curves for fundamental mode Rayleigh waves from recordings of both earthquake and ambient noise sources using the multiple filter analysis (MFT) of Herrmann & Ammon (2004). The fundamental mode is isolated by phase match filtering. Dispersion curves are manually picked from the maximum amplitudes in a plot of group velocity versus period.

Fundamental mode Raleigh waves from earthquakes generate reliable dispersion curves in a band from 5 to 70 s. The minimum period we analyse for ambient noise is 5 s, and the maximum depends on the distance between station pairs. Following Bensen *et al.* (2007), we enforce a minimum interstation spacing of three wavelengths, which, assuming a phase velocity of 4 km s^{-1}, means that the maximum reliable period for group velocity dispersion measurements is $\Delta/12$, where Δ is the interstation distance in km. The maximum station separation limits the maximum period in the ambient noise dispersion curves to 32 s; any dispersion measurements for periods greater than the maximum are discarded.

There is considerable redundancy in paths for both earthquake and ambient noise generated surface waves, which allows us to identify potential outliers by comparing them to path-averaged dispersion curves. For the most part, dispersion curves derived from ambient noise are very similar, as are comparisons between ambient noise and nearby earthquakes. This similarity gives us confidence that the curves we obtain from ambient noise are robust.

A visual comparison of clusters of earthquake generated paths with stations and events lying within 4 per cent of one another revealed 34 paths (or about 2 per cent of the total) with dispersion curves that deviated significantly from the mean. These were treated as outliers and discarded. We note that a similar quality control was used in generating the Acton *et al.* (2010) and Rham (2009) data set.

2.2.2 *Tomographic inversion*

Path-averaged Rayleigh wave group velocity measurements from ambient noise and earthquake sources were combined to invert for Rayleigh wave group velocity maps. We parameterize a region including all sources and receivers (Fig. 4) by a 2-D mesh consisting of nodes of triangular elements with sides 1° in length on a spherical surface using the programme *gmsh* (Geuzaine & Remacle 2009).

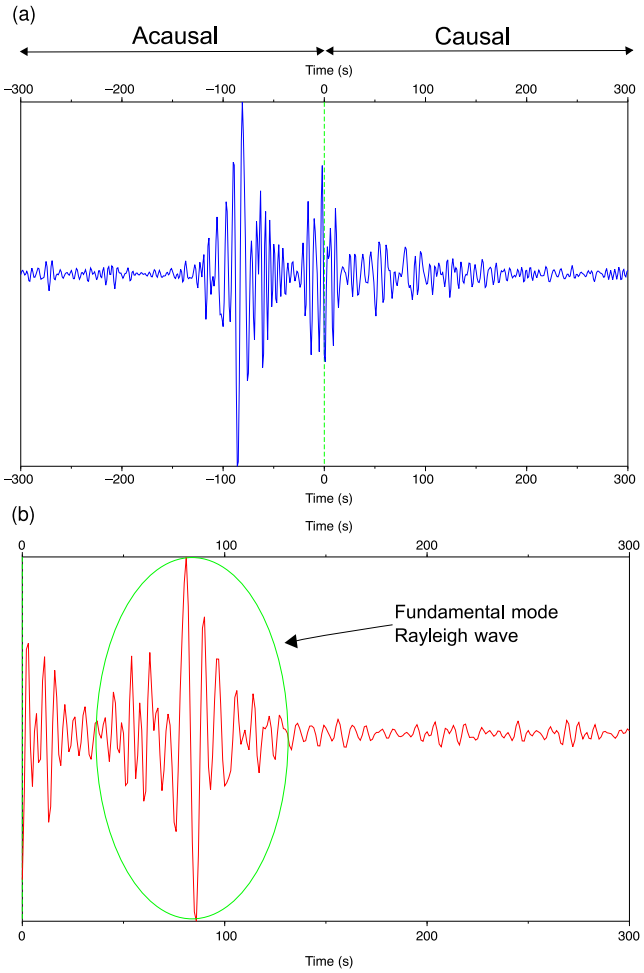

Figure 5. (a) Causal, as if there were an event at KARD, received at KMSK, and acausal, as if there were an event at KMSK, received at KARD, sides of the cross-correlation of vertical component ambient noise data between KARD and KMSK. Asymmetry between the two sides can be clearly seen. (b) Average of the causal and acausal sides of the cross-correlation between KARD and KMSK. The fundamental mode Rayleigh Wave can be clearly seen.

The group slowness at each node was calculated from the dispersion measurements on intersecting propagation paths as described by Mitra *et al.* (2006). We follow Acton *et al.* (2010) in stabilizing the inversion by placing an *a priori* constraint on the standard deviation of the slowness across a reference distance on the grid. We use a reference distance of 10° and an *a priori* standard deviation of 0.045 for each period. Wave speeds within each triangular element are calculated using a three point linear interpolation. Pseudo-dispersion curves were extracted by bicubic interpolation at the mid-point of each bin along the profile (line A–B in Fig. 1).

2.3 Joint inversion

Receiver functions and surface wave dispersion curves have complimentary sensitivities to heterogeneity in the crust and upper mantle. Dispersion curves are sensitive to absolute values of, but not to large gradients in, wave speeds. Receiver functions, on the other hand, are primarily sensitive to large wave speed gradients, but the locations of the gradients depend on the absolute wave speeds. By jointly inverting receiver functions and surface wave dispersion for shear velocity we can reduce their inherent ambiguities while constructing a model that is consistent with both (Özalaybey *et al.* 1997; Juli *et al.* 2000). We use a standard Baysian least-squares method to solve for a 1-D structure under specified points on the surface of the Earth, in this case the mid-point of each bin along the profile, using *P* and *S* receiver functions and fundamental mode Rayleigh wave pseudo-dispersion curves.

Values for V_s, V_p, density and attenuation (Q_a and Q_b) must be specified in our forward modelling, but the inversion is sensitive almost exclusively to V_s. Hence, we adopt a fixed V_p/V_s ratio from Makarov *et al.* (2010) of 1.73 to determine V_p. We use a formula from Roecker *et al.* (2004) to estimate density from V_p. Q_a and Q_b are fixed at 300 and 600, respectively. Receiver functions are computed using a technique based on Haskell (1960, 1962) extended for finite Q in a way similar to that described by Silva (1976). Surface wave dispersion curves are calculated using a locked mode technique based on that described by Gomberg & Masters (1988).

Combining different types of data in a joint inversion requires relative weighting. Tests we performed on regularization and inversion stability suggest that the average normal equation diagonal should not be more than 10 per cent larger than the average inverse covariance matrix diagonal, and we ensure this by weighting the surface wave observations by about a factor of 10 relative to the receiver functions. Sensitivities of the *P* and *S* receiver functions are similar and so are weighted equally. In any event, as the *S* receiver functions did not have a significant impact on the models resulting from the inversion, the choice of weight in this case is relatively inconsequential.

Five inversions are performed for each bin: (1) inversion of surface wave dispersion curves only with a half-space starting model, (2) joint inversion of dispersion curves and *P* receiver functions with a half-space starting model, (3) joint inversion of dispersion curves and *P* receiver functions using the model resulting from the inversion of the dispersion curves with a half-space starting model, (4) joint inversion of dispersion curves, *P* receiver functions, and *S* receiver functions with a half-space starting model and (5) joint inversion of dispersion curves, *P* receiver functions, and *S* receiver functions using the model resulting from the inversion of the dispersion curves only as the starting model. The half-space starting model had a V_s of 4.48 km s^{-1}, corresponding to the uppermost mantle velocities of AK135 (Kennett *et al.* 1995), and is parameterized by 1-km-thick layers from the surface to 300 km depth.

To mitigate short wavelength artefacts not required by the observations, we start by analysing the longest periods and gradually increasing the bandwidth to include the entire frequency band (e.g. Pratt *et al.* 1996). For the inversion of the surface wave dispersion curves only, the bandwidth is initially 70–55 s, then 70–30 s, 70–18 s, and finally the entire range from 70 to 5 s. For the joint inversions the initial bandwidth is 70–10 s and then increased in 0.1 Hz steps to 1.25 s. Because surface waves have much more energy at long periods, this strategy means we start by inverting predominantly surface wave dispersion curves and gradually including more contributions from the receiver functions.

3 RESULTS

3.1 Stacked receiver functions

A section of stacked *P* receiver functions along the profile A–B (Fig. 6) shows a coherent conversion with variations in delay time of between 5 and 9 s across the range. The longest delay times are

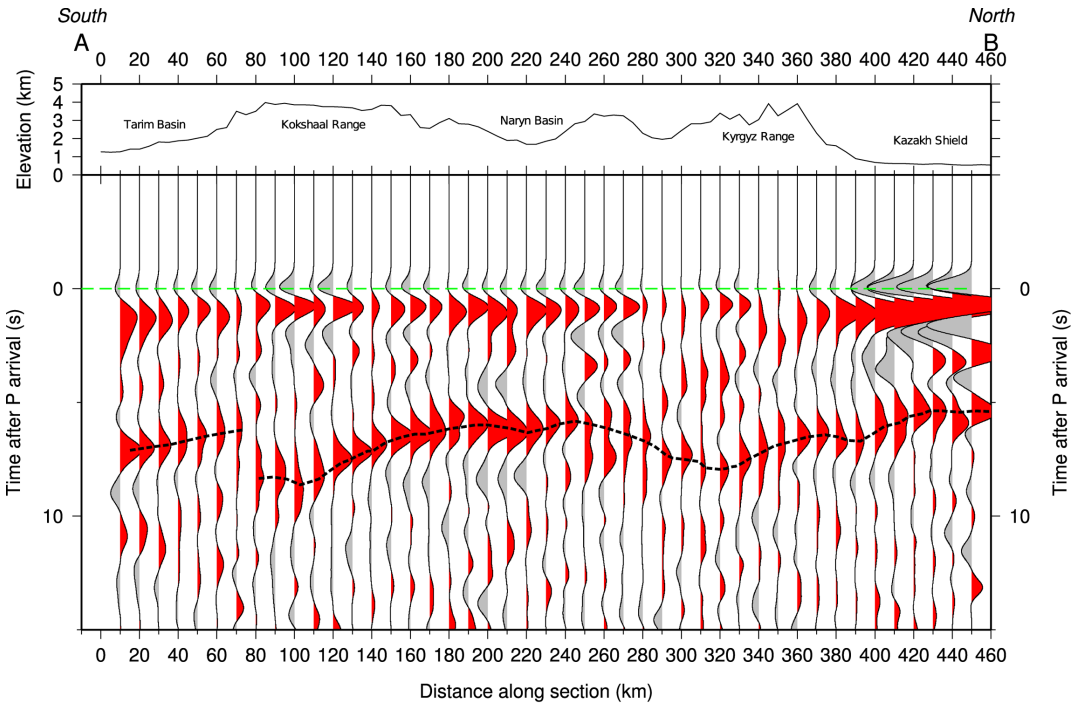

Figure 6. Stacked *P* receiver functions. Coherent *P*-to-*S* conversions at 5–9 s are observed. Arrival times varying across the range; the longest arrival times are observed beneath the Kokshaal range, while the shortest arrival times are beneath the Naryn Valley and Kazakh Shield. The signal at this time is dominated by an apparent conversion from the Moho, but also contains contributions from crustal multiples. A strong conversion is also seen at 1s, likely from the base of the sedimentary layer.

located beneath the Kokshaal and Kyrgyz ranges, while the shortest are found beneath the Kazakh shield and the Naryn Valley. While the origin of this conversion is uncertain, we simply note at this stage that the delay times are in the range of what would be expected for a *P*-to-*S* conversion from the Moho. There is another strong arrival at 1 s for many of the bins, apparently from a conversion in the uppermost crust, that again can be traced coherently across most of the range. The amplitude of this arrival is largest in the northern part of the section, beneath the Chu Basin, where Cenozoic sedimentary deposits are up to 4 km thick (Laske & Masters 1997).

A similar coherent conversion is found in the stacked *S* receiver functions along the profile between 7 and 9 s in bins 110–310 (Fig. 7). Like the stacked *P* receiver functions, the longest delay times are beneath the Kokshaal and Krygyz ranges (near bins 110 and 300) and the shortest beneath the Naryn Valley (bin 220). Unlike the *P* receiver functions, there is no converted phase signal around the 1 s delay time. This may be due to the lower frequency content of *S* receiver function that makes it more difficult to resolve velocity contrasts in the uppermost crust.

3.2 Rayleigh wave tomography maps

Group velocity maps were obtained for periods from 5 to 70 s (Fig. 8a). There is a strong correlation at shorter periods with surface geology, in particular with regions of large sediment thickness (Laske & Masters 1997) shown in (Fig. 8b). The slowest velocities are observed in the Tarim Basin, where there are more than 6 km of sediments (Allen *et al.* 1999) and in the Fergana Basin, which has a sediment thickness of 8 km (Laske & Masters 1997). The fastest velocities are observed beneath the Pamirs and the Tien Shan. This correlation persists at periods of 15–30 s, although the faster velocities in the Tien Shan are concentrated in the vicinity of the profile, with higher velocities at 15–20 s periods beneath the Kokshaal and Kyrgyz ranges than beneath the Naryn Valley. At periods of 40–70 s, velocities along the line of section are slower in the south than in the north. They are also slow beneath the Pamirs and fast beneath the Tarim Basin.

3.2.1 Resolution of group velocity maps

We performed checkerboard tests with elements of 2°, 3° and 5° dimension to estimate the spacial resolution and recovery of the group velocity inversion. Based on values determined in the actual group velocity maps, shear wave speeds in the checkers are perturbed by ±23 per cent, corresponding to a range from 2.5 to 4 km s^{-1}. Synthetic group velocity measurements and maps were calculated for the models using the same paths as in the real data.

Checkerboards with elements of 3° and 5° dimension are well resolved by 10 s Rayleigh waves across the Kygyz Tien Shan and surrounding regions (Fig. 9). At 2° dimension, the checkerboards are moderately well resolved throughout most of the region south of 43°N, reflecting the poorer path coverage to the north. The 2° dimension represents the limit of what can be resolved by the inversion using a grid with elements made of 1° length sides, but features such as the sedimentary basins that we would hope to be able to resolve at 10 s are around 2° or larger in size. In all of the checkerboard tests there are differences in amplitudes of the model used to generate the synthetics. South of 43°N the differences are small, being 91 per cent or more of the true amplitude for 3° and 5° checkers, and 87 per cent or more for the 2° checkers.

3.3 Shear wave velocity structure

We create 2-D velocity depth images along the azimuth of the MANAS line by combining 1-D velocity models obtained from

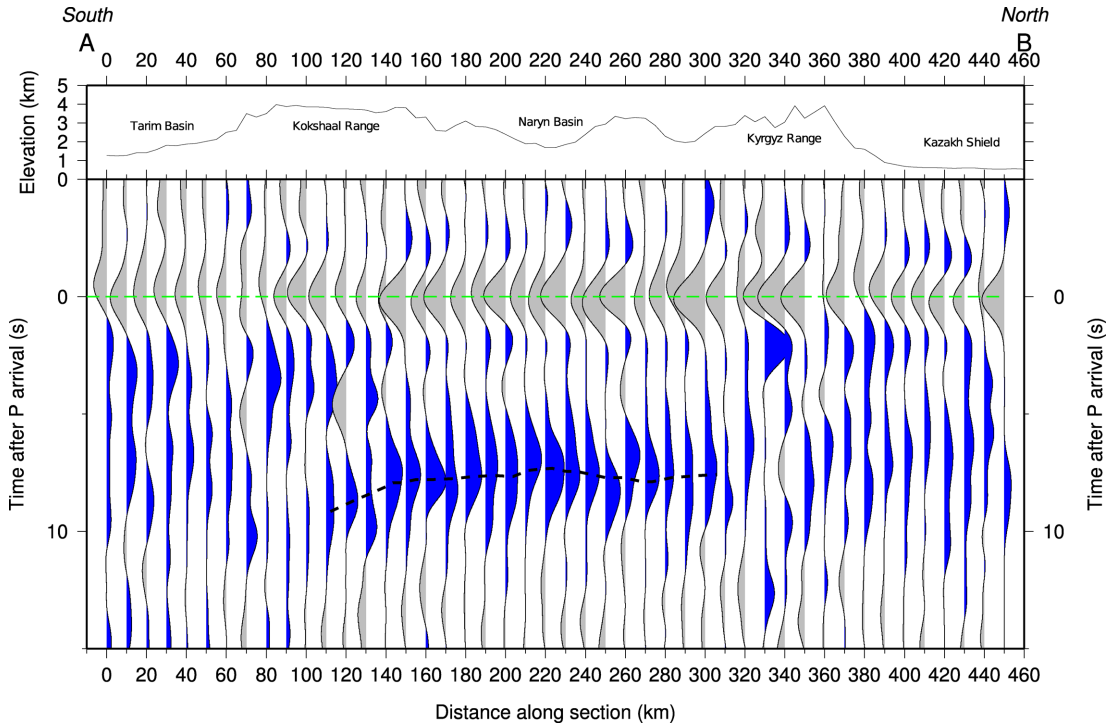

Figure 7. Stacked *S* receiver functions. Time and amplitude reversed to allow for easy comparison with PRFs. Coherent *S*-to-*P* conversion can be seen in the middle of the range at arrival times of 7 and 9 s which agree with conversion seen in the PRFs. These are likely to be conversions from the Moho.

the inversion of dispersion curves derived from the group velocity maps sampled in each bin, along with the *P* and *S* receiver functions that have piercing points in the same bin. We inverted the dispersion curves by themselves (Fig. 10a), and jointly with *P* and/or *S* receiver functions (Figs 10b–e). We carried out inversions starting from a half-space (Figs 10a, b and d) and from the best-fitting surface wave model (Figs 10c and e).

To first order, these images are quite similar to each other; the surface wave only model (Fig. 10a) looks like a smoothed version of the joint surface wave and receiver function models. To some extent this is not surprising, partly because of the higher frequency content of the receiver functions but also because the surface wave dispersion curves are derived from slowly varying group velocity maps. This is particularly true at depths greater than about 50 km where the models are bimodal, with slower velocities beneath and south of the Kokshaal range, and higher velocities beneath the Naryn Valley and north to the Kazakh shield. These trends are evident in the group velocity maps for periods greater than 40 s (Fig. 8).

The models that result from the joint inversion of surface waves and *P* and *S* receiver functions are not significantly different from those derived from the joint inversion of surface waves and *P* receiver functions. While the general trends in lateral wave speed variations in the joint inversions are similar to those in the surface wave only inversions, in the upper 50 km the receiver functions add considerable detail in vertical variations. This is particularly true in the upper 20 km of the southern part of the profile where an additional narrow wave speed reversal is defined at about 10 km depth and the contrasts associated with a reversal at about 15 km depth are amplified.

We note that, in all of these images, the sub-Moho shear wave velocities are slower than one might expect. For example, despite that fact that our starting model was a half-space of 4.48 km s^{-1}, wave speeds that one usually associates with the mantle are found north of the Naryn Valley only at depths greater than than about 65 km. We choose the 4 km s^{-1} contour to represent the transition from the crust to the mantle as the surface waves sensitive to this depth are not able to resolve a sharp discontinuity such as the Moho: the wave speed model that results from the inversion will have low velocities because the lower crust will smear into the uppermost mantle. We identify the Moho depth from the inflection point of the shear velocity versus depth curve and the depth of the Moho determined from previous receiver function studies. (e.g. Fig. 10a). The 4 km s^{-1} contour as a proxy for the Moho is in agreement with the velocity contour chosen by Acton *et al.* (2010) for much of the rest of Asia.

The wave speed models shown in Fig. 10 predict the 1-D fundamental mode Rayleigh wave dispersion curves and *P* receiver functions used in the inversions quite well; representative fits for bins 110 and 270 are shown in Figs 11 and 12. In comparison to the misfit associated with the half-space starting model, these represent significant reductions in misfit (Table 1). The fit to the *S* receiver functions, as can be seen in Figs 11 and 12, generally is poor. The rms misfits for the *S* receiver functions do not improve from the half-space with further iterations, although the inclusion of the *S* receiver functions in the joint inversions does improve the overall misfit (Table 2).

We note that the velocity models in bin 110 from inversions that include receiver functions have several sharp velocity gradients in the upper crust that are not seen in the velocity model resulting from the inversion of surface wave data alone. Synthetic dispersion curves generated in these two models show little difference, indicating that the surface waves are not sensitive to these gradients. Nevertheless, the rms misfit to the surface wave dispersion curves is slightly better in the model generated jointly with receiver functions. On the other hand, the synthetic *P* receiver function produced using the model obtained from the inversion of just surface wave data fits the *P* receiver function data poorly. (See Figs S4 and S5).

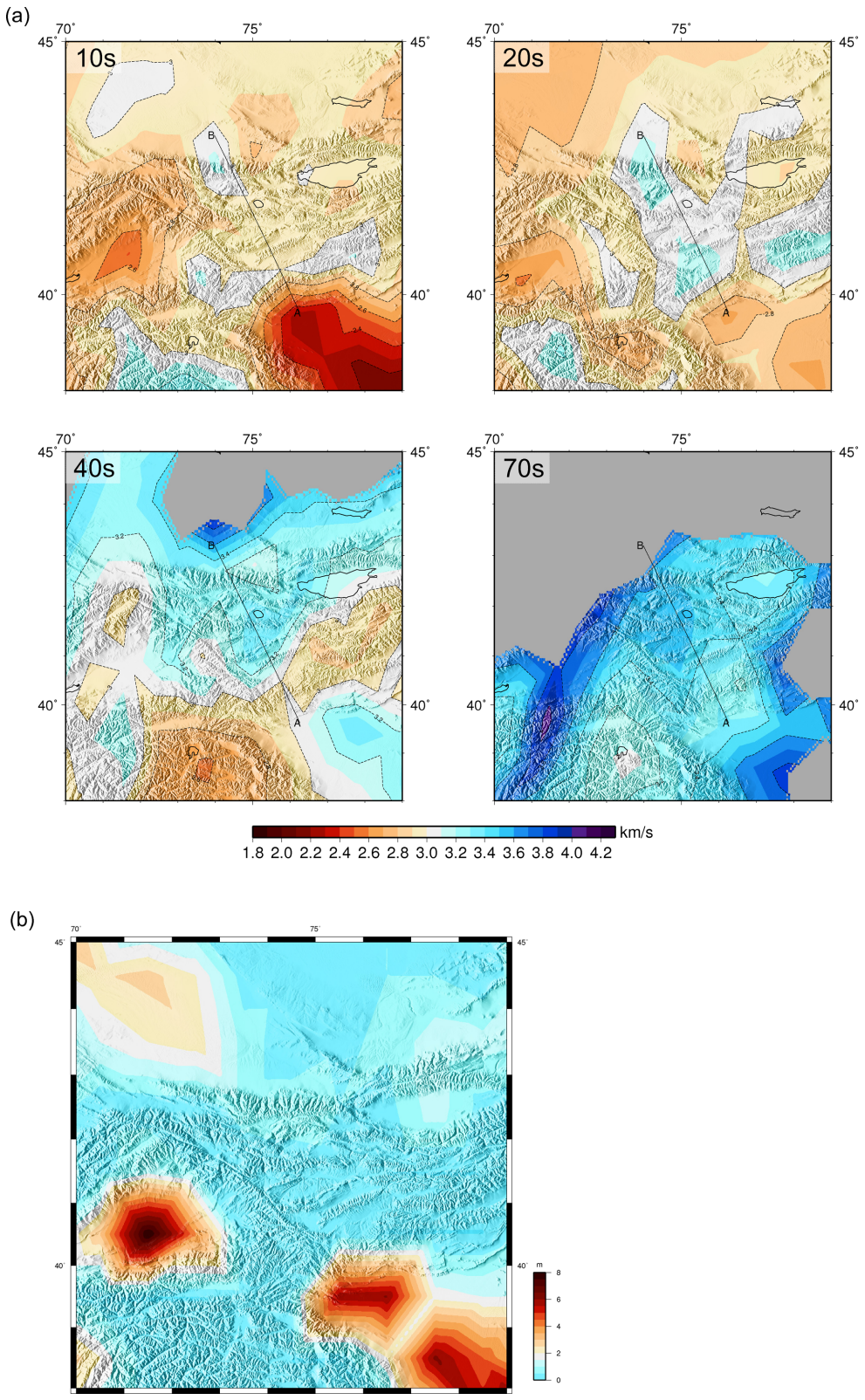

Figure 8. Fundamental mode Rayleigh wave group velocity maps for 10, 20, 40 and 70 s periods for the region around the MANAS array. The same scale is used in all of the maps. Grey areas are where the errors in the group velocities are greater than 0.3 km s^{-1}. (b) Sediment thickness map showing the same area as (a) with data from the Global Map of Sediment Thickness, Laske & Masters (1997).

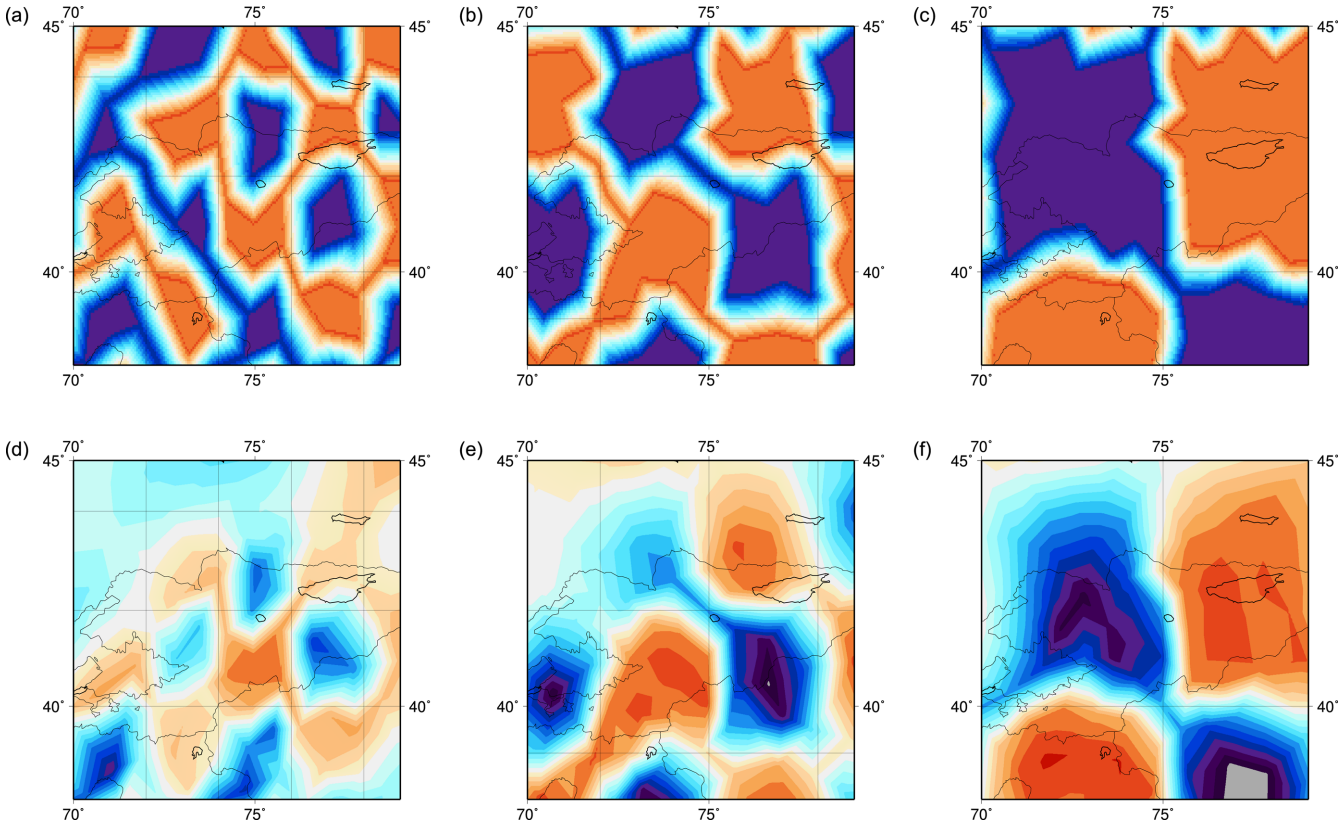

Figure 9. Checkerboard tests for 10 s Rayleigh wave group velocity maps for the region shown in Fig. 8 with (a) 2°, (b) 3° and (c) 5° checkerboards. (d)–(f) are the corresponding recovery maps produced by inverting the synthetic traveltimes derived from the checkerboard models for the paths shown in Fig. 8 which were used in the fundamental mode Rayleigh wave group velocity tomographic inversion.

P receiver functions are well fit to delay times of 15 s after the *P* arrival in the each of the models that result from joint inversion of surface waves and *P* receiver functions (Figs 11 and 12). By contrast, the fit to the *S* receiver functions is poor, and there are features in the *S* receiver functions that are difficult to reconcile with the *P* receiver functions and surface wave dispersion curves. In particular, there is a large positive signal around the *S* arrival time in the observed *S* receiver function where the synthetics predict a negative. The reason for this discrepancy is not clear, but we suspect it is due to a combination of noise in the SRF and perhaps the appropriateness of using the Farra & Vinnik (2000) scheme in deconvolving the SRF for this particular application.

3.4 Reliability of features in velocity models

To estimate the robustness of various features in the velocity models, we generate synthetic dispersion curves and receiver functions in trial models that do not include them. The motivation is to quantify the sensitivity of the data to features of particular interest; if the data can be fit more or less equally well without including a feature, it is considered insignificant.

Two features of particular interest are the low velocities beneath the Kokshaal range at depths of 60 km, and the relatively high velocities north of the Naryn Valley at about 70 km depth. Both of these features are suggested by the group velocity maps (Fig. 8) and, indeed, a model constructed without them gives dispersion curves that deviate significantly from the observed velocity curve (see Figs S1 and S2).

For *P* receiver functions, there is a possibility that later arrivals are multiples of conversions at shallow depth. For example, in bin 110 we find (see Fig. S3) that the relatively large velocity contrast at around 20 km produces a multiple which arrives at a similar delay time to the conversions from the broad velocity increase at depths greater than 60 km. The conversion from the gradient below ∼60 km is above the noise, however the signal observed at a similar time (around 8 s) in the data and synthetic receiver functions could be the result of interference between the multiple from an upper crustal velocity contrast and the conversion from the gradient below 60 km. The *S* receiver functions do not have the problem of interference between signals from converted phases and those from multiples, and so it is possible to say with more certainty that particular signals are a result of particular velocity gradients. For example, the negative signal seen in bin 270 in the synthetic *S* receiver functions around 8 s is most likely due to the increase in velocities between 50 and 70 km.

There are several sharp gradients in velocity in the upper 20 km that appear in the receiver function images that are not required by the dispersion curves (i.e. surface waves are not sensitive to them). To show that these are not simple artefacts, we calculate synthetics to identify which gradient in the velocity model is responsible for the conversions. For both bins 110 and 270 the velocity increase at 3 km produces a large signal around 1 s after the *P* arrival in the *P* receiver functions. This signal is seen in the majority of the stacked *P* receiver functions, and is particularly strong in the stacks for bins in the Kazakh Shield. Deeper velocity gradients are observed in the upper crust and produce signals between 1 and 4 s after the *P* arrival time. In the *S* receiver functions the velocity

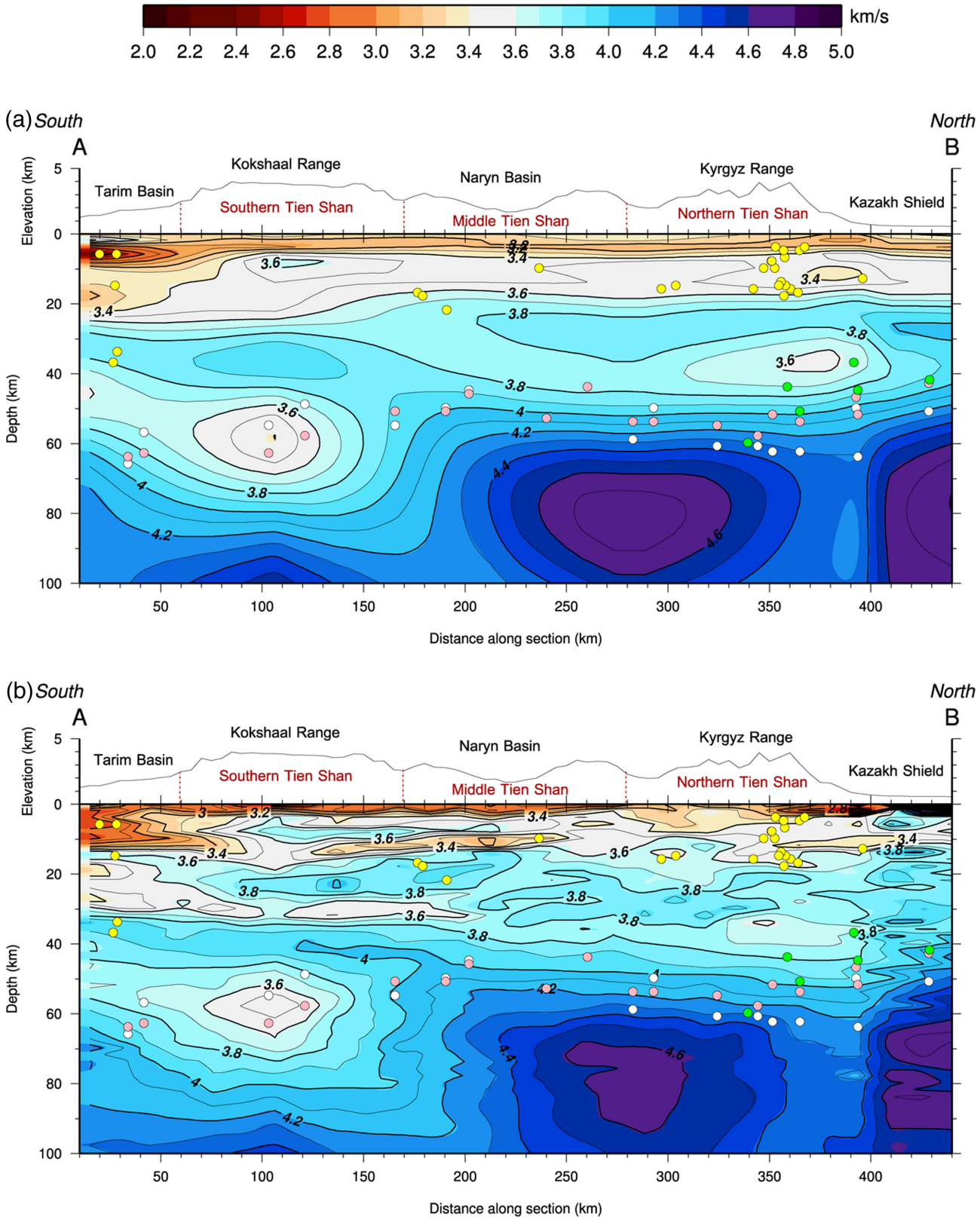

Figure 10. Shear wave speed V_s depth along the line A-B. Profile topography is plotted above each section. Yellow circles are earthquake locations from Sloan *et al.* (2011). The green circles are the depths of the Moho from stations from Bump & Sheehan (1998), the white circles are the Moho depths from Vinnik *et al.* (2004), and the pink circles are Moho depths from Vinnik *et al.* (2006). (a) is from inversion of 1-D fundamental mode Rayleigh wave data, using a mantle half-space starting model, (b) from the joint inversion of 1-D fundamental mode Rayleigh wave data and stacked *P* receiver functions for each bin, using a mantle half-space starting model, (c) joint inversion of 1-D fundamental mode Rayleigh wave data and stacked *P* receiver functions for each bin, using the velocity model in (a) as the starting model, (d) joint inversion of 1-D fundamental mode Rayleigh wave data and stacked *S* receiver functions and *P* receiver functions for each bin using a mantle half-space starting model and (e) joint inversion of 1-D fundamental mode Rayleigh wave data and stacked *S* receiver functions and *P* receiver functions for each bin, using the velocity model in (a) as the starting model.

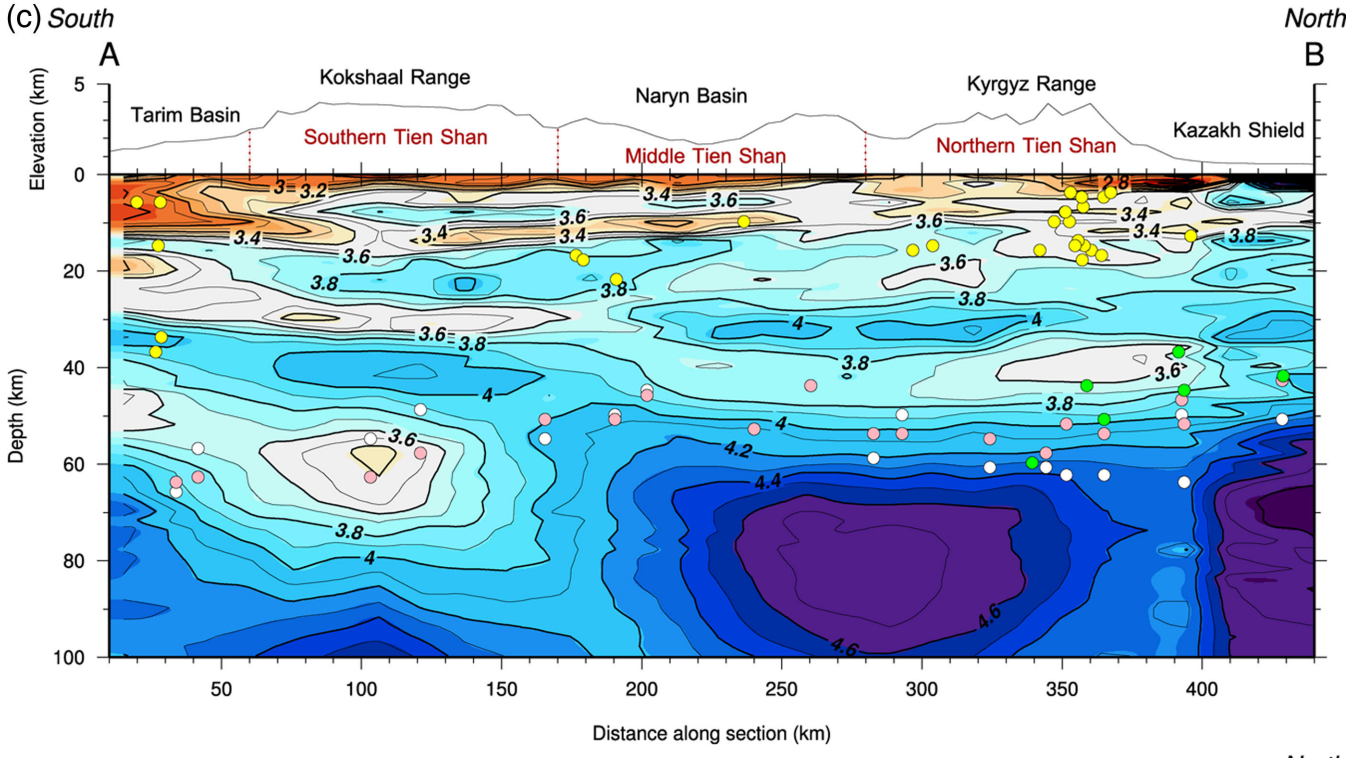

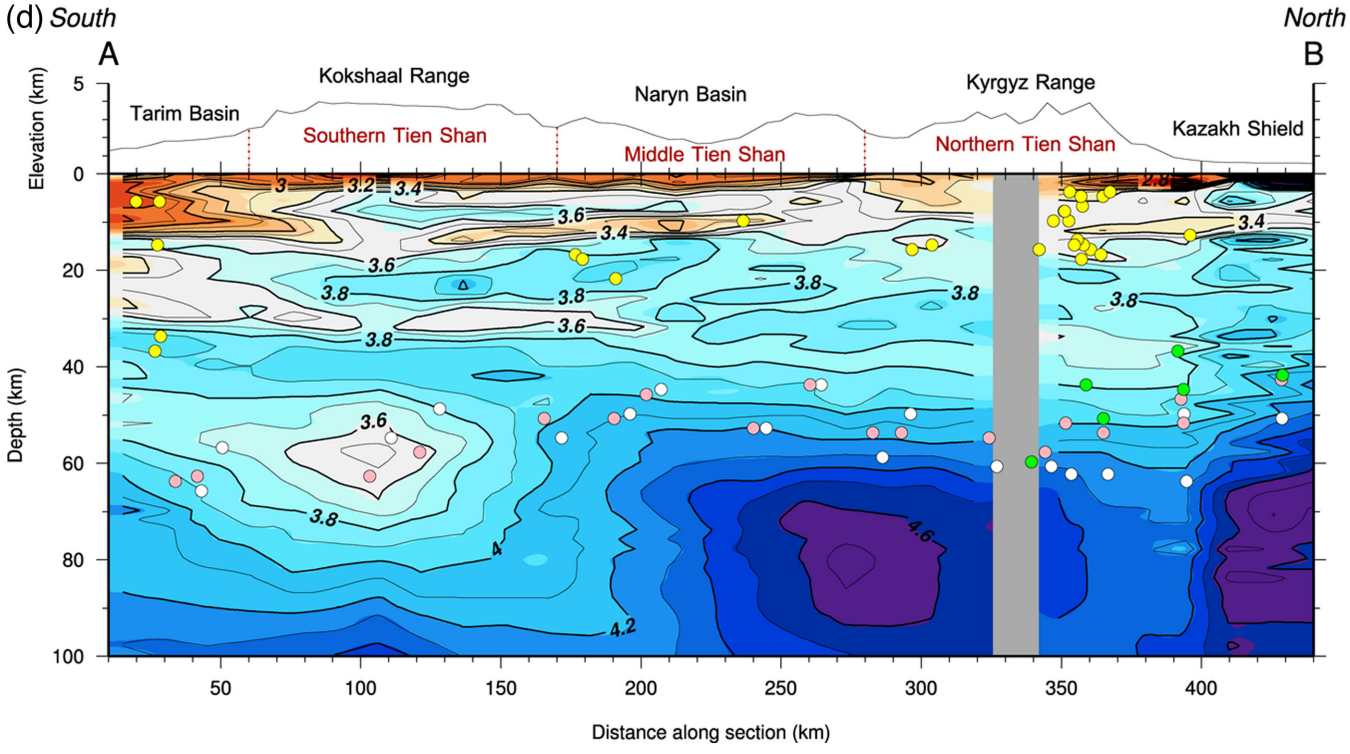

Figure 10. (*Continued.*)

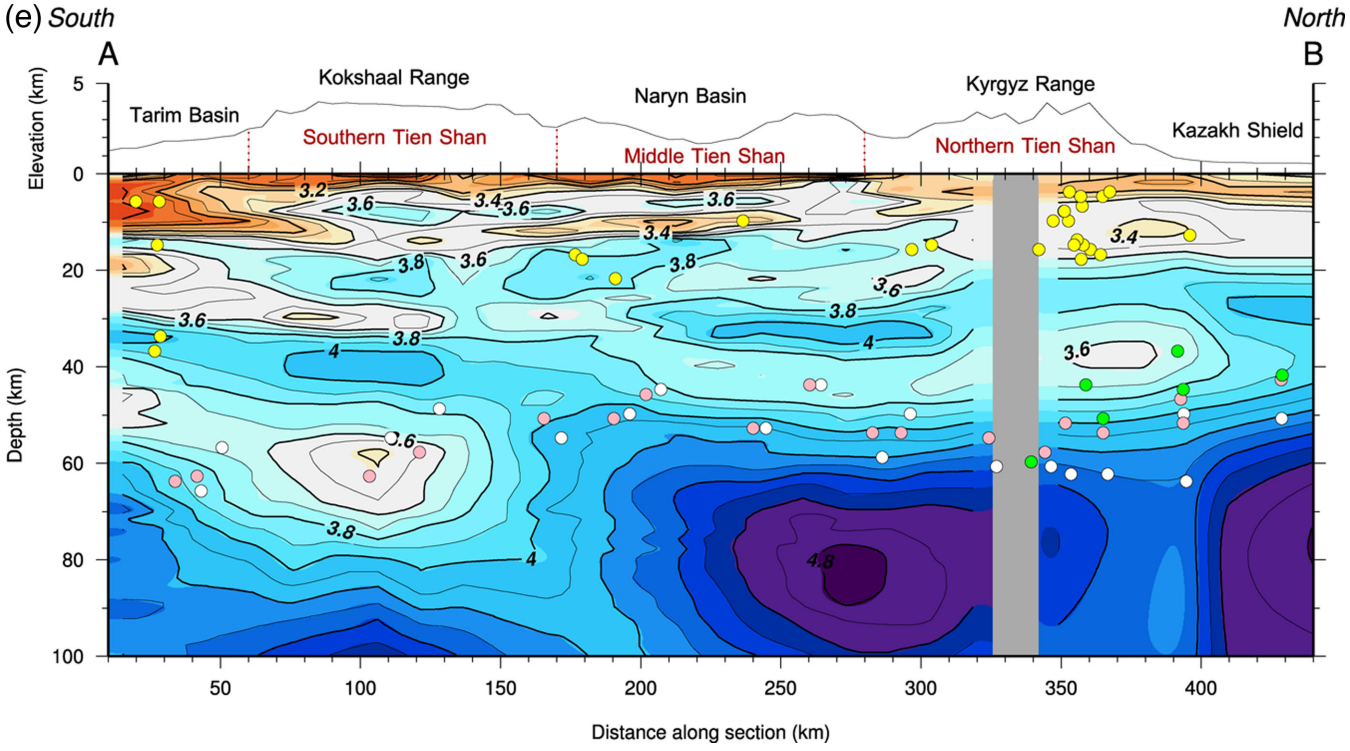

Figure 10. (*Continued.*)

gradients in the upper crust result in signals between 0 and 4 s before the *S* arrival, which constructively interfere and result in a negative signal arriving just before the *S* arrival time. Multiples from these converted phases are seen after the *S* arrival time.

4 DISCUSSION

We consider the features discussed in Section 3.4 to be robust. Moreover, it is clear that by jointly inverting surface wave dispersion curves and *P* receiver functions we can recover information about the V_s structure to which the surface waves on their own are not particularly sensitive, while preserving the overall trends in absolute V_s that they require. It does not appear that including *S* receiver functions into the inversion adds much information, although it does decrease the overall misfit.

Based on the depth of the Moho previously observed in this region from receiver function studies (Bump & Sheehan 1998; Vinnik *et al.* 2004, 2006), and, as described by Acton *et al.* (2010) for much of the rest of Asia, we adopt the 4 km s^{-1} contour as a proxy for the Moho discontinuity. Based on this choice, we infer that all the earthquakes observed by Sloan *et al.* (2011) occur within the crust. We also infer that the crust has a nearly uniform thickness north of the Naryn Valley. This is a significantly different interpretation of Moho depth than that proposed by previous studies (Vinnik *et al.* 2004, 2006). At first this would appear to be inconsistent with the pattern of delay times shown in Figs 6 and 7, which suggest that the Moho deepens beneath the Kyrgyz Range and shallows beneath the Naryn Valley, however the synthetic *P* receiver functions produced by this model (Fig. 13) can produce a pattern of delay times which is very similar to that shown in Fig. 6.

As mentioned earlier, interference between primary conversions and multiples from impedance contrasts in the upper crust can result in amplification or attenuation of a later signal, such as a converted phase from the Moho. Given the strong contrasts in wave speed we observe in the upper crust, it is important to understand how each of them contributes to the overall receiver function, rather than simply concluding that a coherent signal at a reasonable delay time is from the Moho. For example, the stacked *P* receiver function in bin 320 beneath the Kyrgyz range shows a positive signal at 8 s, which would suggest that the Moho is about 60–70 km depth. However, both the 4 km s^{-1} contour and the steepest velocity gradient in the velocity model from the inversions are around 50–56 km depth. Synthetic receiver functions (Fig. 14) show that the velocity increase at 50–56 km produces a conversion at around 6 s, but also that multiples from a velocity increase at 12 km and a velocity decrease at 17 km result in a negative signal at around the same time. This essentially eliminates the mode conversion from the actual Moho, and instead we observe a small negative signal at around 6 s. The remaining signal observed at 8 s is from a deeper velocity increase at 60–72 km.

This result highlights an additional benefit of joint inversion of surface waves and receiver functions, in that not only are the apparent phase conversions in receiver functions migrated to an appropriate depth by the absolute velocities derived from surface waves, but consistency between data sets can reveal the effects of interference between primary and multiple phase conversions in amplifying or eliminating these phases.

At the southern boundary of the Tien Shan, beneath the Kokshaal Range, crustal wave speeds are found as deep as 75 km. One would expect greater crustal thickness beneath the Kokshaal from isostacy, but the wave speed reversal, seen in all models, at about 45 km depth is not consistent with a scenario of simple thickening by crustal shortening. Instead, it appears that upper crustal type lithologies have been displaced to mantle depths, presumably from the south. This interpretation aligns with those made by

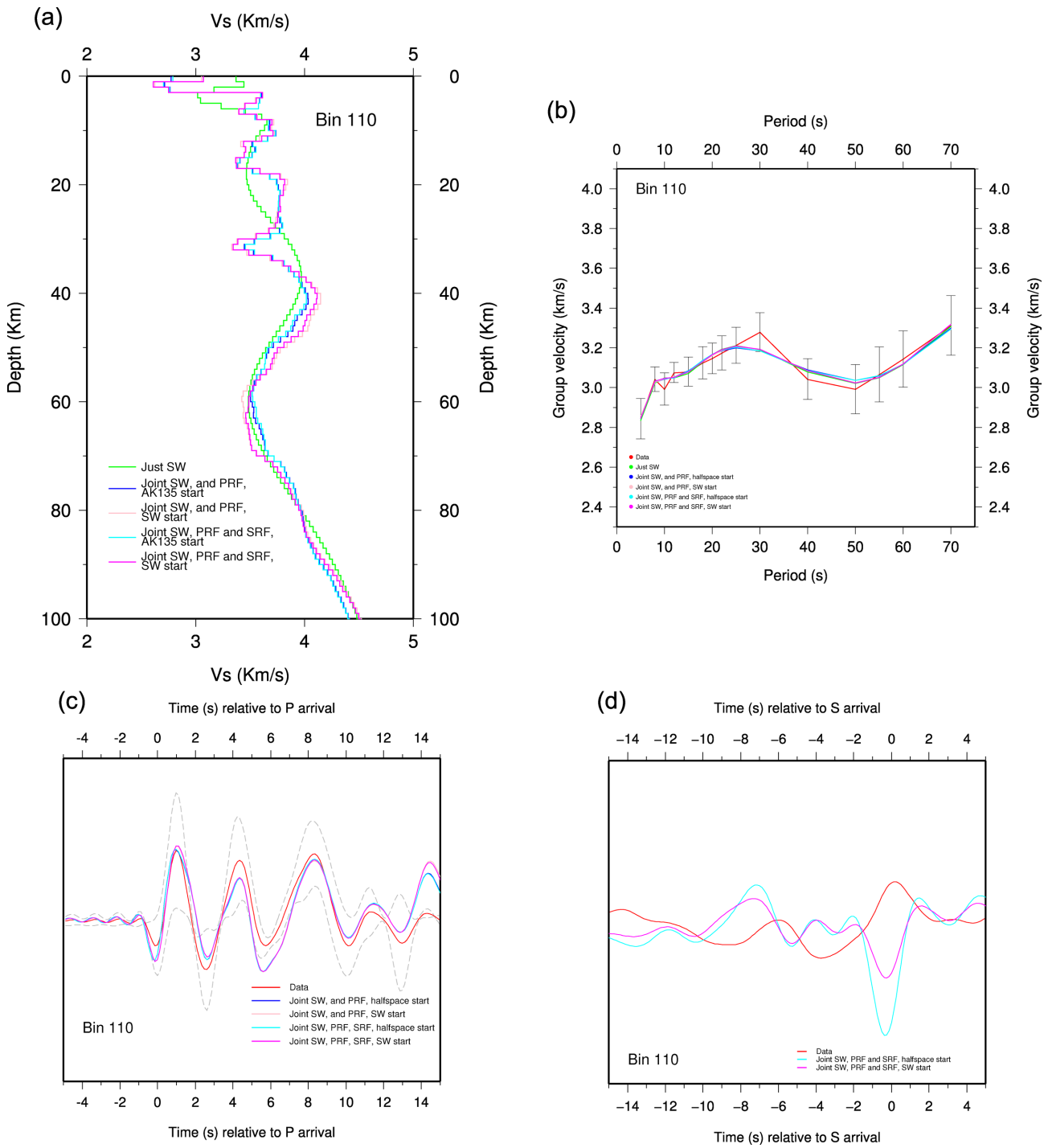

Figure 11. (a) Velocity structures from each of the five inversions in bin 110, 110 km along the line A–B. (b) Data and synthetic group velocity curves for bin 110. (c) Data and synthetic *P* receiver functions for bin 110. Grey dashed lines are one standard deviation. (d) Data and synthetic *S* receiver functions for bin 110.

previous studies (Poupinet *et al.* 2002; Vinnik *et al.* 2006; Makarov *et al.* 2010) that the Tarim Basin underthrusts the Tien Shan. The lateral extent of the thickened crust, to around 160 km along section or about 100 km north of the boundary between the Tarim Basin and the Tien Shan, agrees with the distance (50–100 km) that Makarov *et al.* (2010) infer from their study of active source data from the MANAS project. Vinnik *et al.* (2006) also observe thicker crust in the southern Tien Shan, although somewhat thinner (60 km) than observed in this study, and also suggest that the greater thickness has resulted from underthrusting of the Tarim Basin. The results of this study, therefore, support the plate model of intracontinental convergence.

Because the limited bandwidth of our signal, the actual Moho could be sharper than it appears in these models. Nevertheless, the velocity models suggest that the Moho transition zone beneath the Kokshaal Range occurs over a large depth range, so the amplitude of the mode conversions in the receiver functions should be relatively low. This may explain why it is not possible to coherently trace

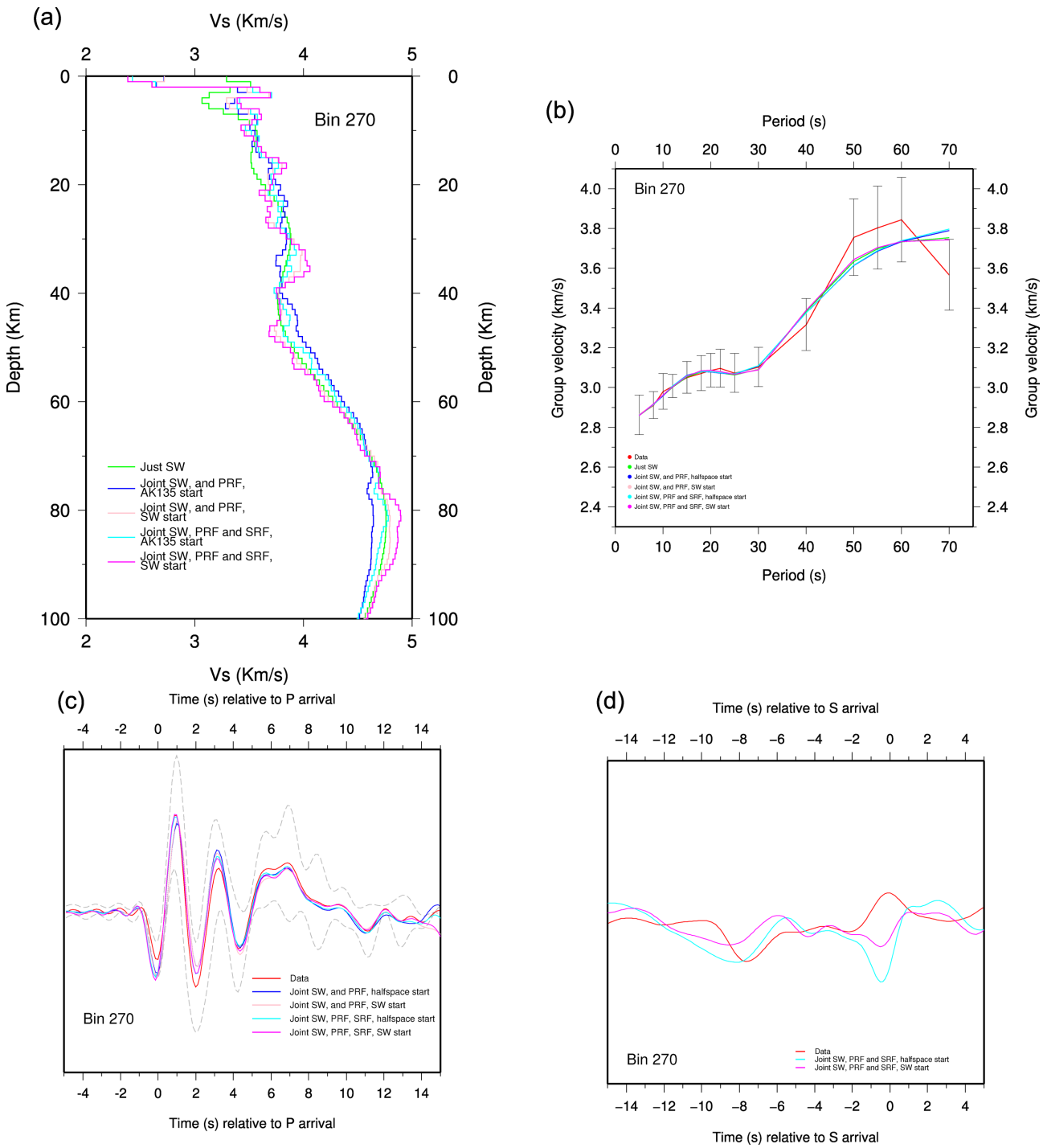

Figure 12. (a) Velocity structures from each of the five inversions in bin 270, 270 km along the line A–B. (b) Data and synthetic group velocity curves for bin 270. (c) Data and synthetic *P* receiver functions for bin 270. Grey dashed lines are one standard deviation. (d) Data and synthetic *S* receiver functions for bin 270.

Table 1. Percentage reduction in misfit to the data with respect to the misfit associated with the half-space starting model.

	Bin 110	Bin 270
Group velocity dispersion curves (all inversions)	98 per cent	92 per cent
P receiver functions (inversions 2 and 3)	61 per cent	75 per cent
P receiver function (inverions 4 and 5)	82 per cent	89 per cent

Table 2. Percentage reduction in misfit to the data from the joint inversion of surface wave, and *P* and *S* receiver functions with respect to the misfit associated with final model from the joint inversion of surface wave and *P* receiver function data.

	Bin 110	Bin 270
Overall misfit (inversion 4 versus inversion 2)	52 per cent	56 per cent
Overall misfit (inversion 5 versus inversion 3)	45 per cent	51 per cent

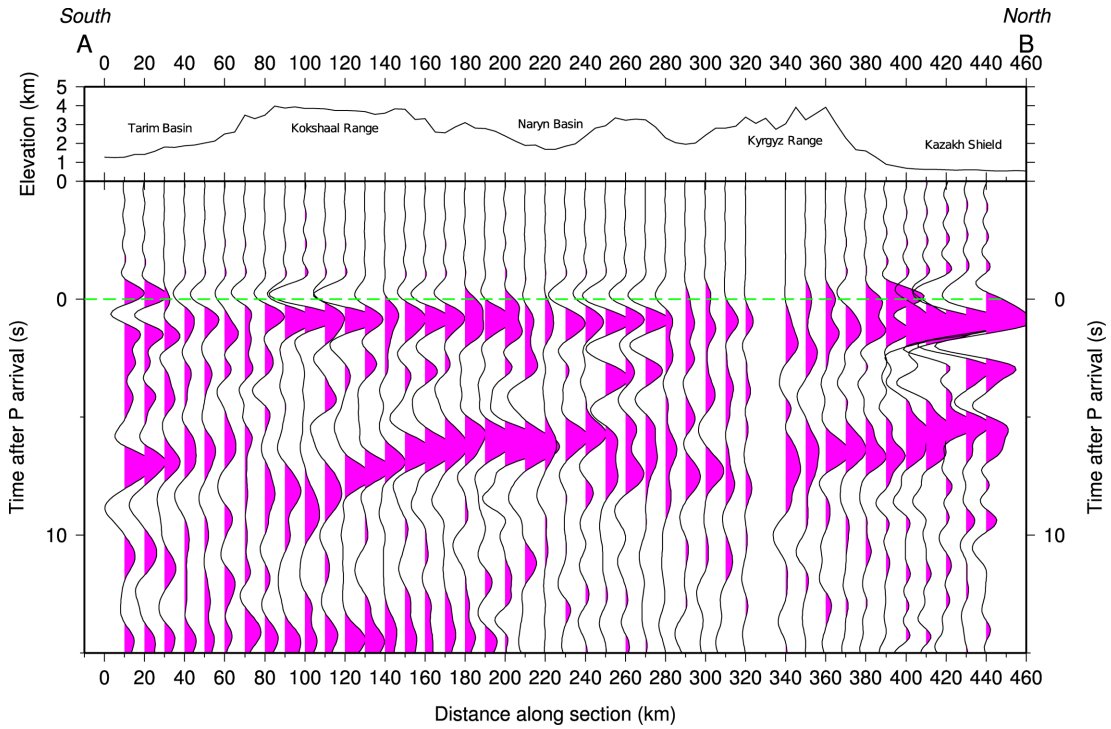

Figure 13. Synthetic *P* receiver functions from the velocity model shown in Fig. 10(e). The arrival times show a similar pattern to those shown in Fig. 6; the longest arrival times are observed beneath the Kokshaal Range, while the shortest arrival times are beneath the Naryn Valley and Kazakh Shield.

a signal in the *S* receiver functions from the southern part of the section; the amplitude is insufficient to confidently interpret the mode conversions above the noise or any other signal. While it is possible to trace a coherent signal in the *P* receiver functions, potential contributions from multiples makes a simple interpretation ambiguous.

The high velocity region in the upper mantle north of Naryn Valley could be the remains of a lithospheric lid, as inferred by Oreshin *et al.* (2002). They suggest that such a lithospheric lid may serve as means of stress transfer across the range, inhibiting shortening. Observations of similar high velocity regions in the upper mantle have been observed in other geophysical studies in the Tien Shan; Vinnik *et al.* (2006) observe several which correspond to depressions, including the Naryn Valley. While a high velocity body is found beneath the northern part of the Naryn Valley, it is centred beneath the ranges to the north, and so a causal link between shortening in the Naryn Valley and the high velocity lid is not required by the results of this study. Oreshin *et al.* (2002) also observe that the high velocity lid in the upper mantle is underlain by a lower velocities. While there are some indications in this study that velocities are lower beneath the high velocity lid, the data used in the inversion are not sensitive to structure below around 100 km depth.

The differences between the velocity structure beneath the Southern Tien Shan and that beneath the Central and Northern Tien Shan may be due primarily to the heterogeneous nature of the crust in this region. The crust where the Tien Shan is now found formed in the Palaeozoic through the accretion of microcontinents (Burtman 1975; Windley *et al.* 1990) that are represented in present-day terranes (Southern, Central and Northern Tien Shan). It may be that some of the differences in the crust and upper mantle persist from the Palaeozoic, and are responsible for in the velocity structures we observe. Notably, the northern limit of the thickest crust is approximately coincidental with the fault separating the Southern and Central Tien Shan terranes. The underthrusting of the Tarim Basin beneath the southern Tien Shan may also be occurring along structures inherited from the Palaeozoic collisions and orogenesis. It may be that the southern edge of the lithospheric lid we observe in the north is where the subducted Tarim Basin butts up against the lithosphere of the Kazakh Shield (see cartoon in Fig. 15). Hence, remnant Palaeozoic structures may have contributed to the formation of the Tien Shan, distant from the current boundary between India and Eurasia.

5 CONCLUSIONS

In this study, we have jointly inverted new data sets for this region to obtain a shear velocity model that provides a better estimate of the velocity structure for the crust and uppermost mantle of the Kyrgyz Tien Shan than was previously available. The results are in reasonable agreement with the results of previous geophysical studies in this area. In particular, we observe the thickest crust beneath the Southern Tien Shan, which we believe to be a result of underthrusting of the Tarim Basin beneath the Tien Shan, and so supporting a plate boundary model of intracontinental convergence (Fig. 15). A lithospheric lid in the uppermost mantle beneath the northern part of the range may have inhibited some crustal shortening in this part of the Tien Shan. This may help to explain why the crust beneath the Central and Northern Tien Shan is thinner than in the south of the range. The observation that the lithospheric lid extends only halfway across the range may resolve the discrepancy between studies which image a high velocity lid and those that do not: it is simply a result of where previous studies have imaged. The crust under the Naryn Valley does not appear to be as thin as reported in previous studies, indicating that it has undergone some shortening. This observation is consistent with the observation that shortening in the Naryn Valley is active.

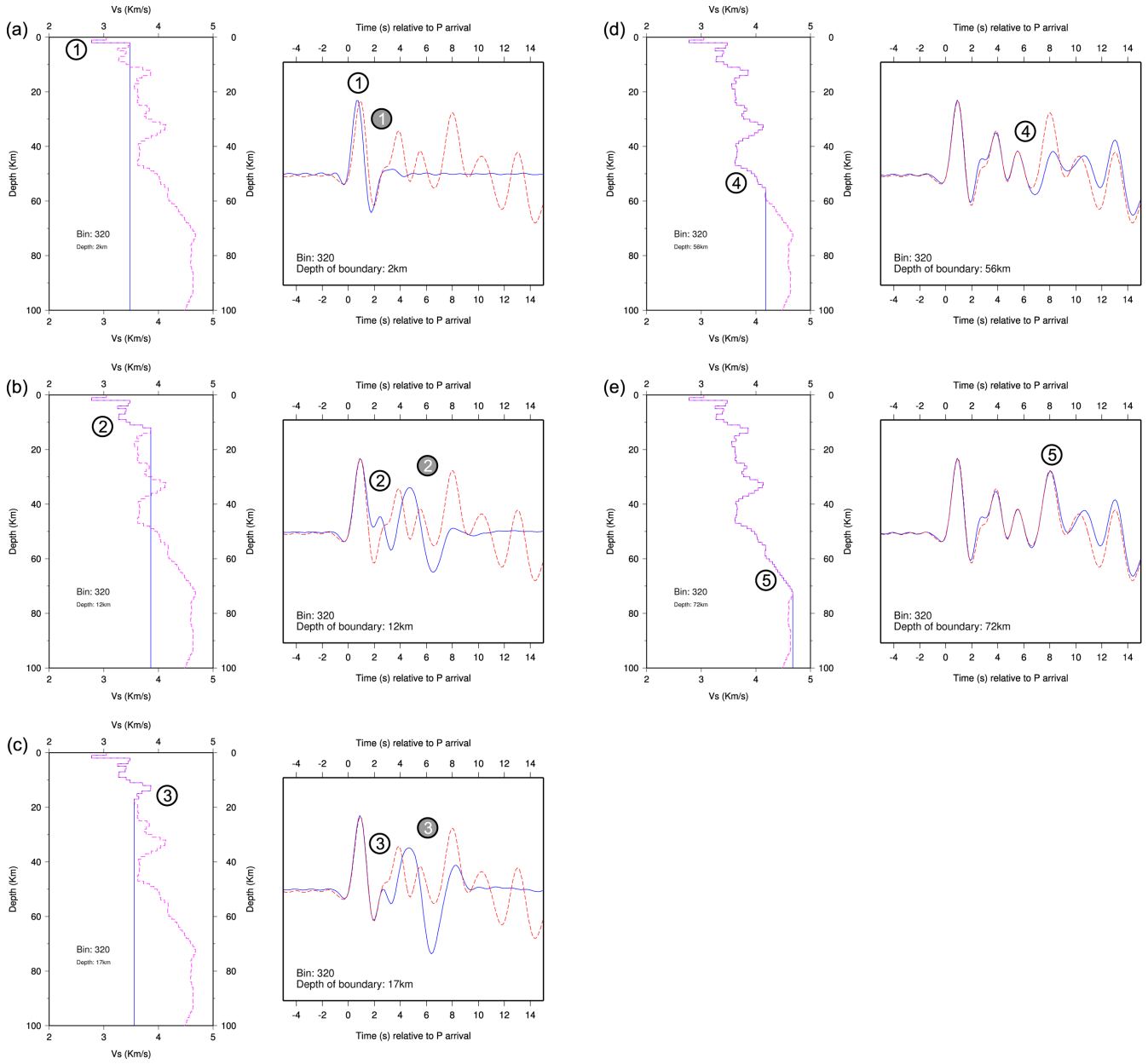

Figure 14. Velocity models (left-hand panel) and *P* receiver functions (right-hand panel) for bin 320. The receiver function shown in blue in (a) is that produced by the velocity model shown in blue in (a), that is the same as the model (shown in pink dashed line) produced from the joint inversion of surface wave, PRF and SRF data with a surface wave starting model up to 2 km depth and uniform below that. The receiver function shown in the red dashed line is that produced by the model resulting from the joint inversion of surface wave, PRF and SRF data. The white circled numbers label, in the velocity model, the velocity contrast of interest, and in the receiver function, the resultant *P*-to-*S* conversion from this velocity contrast. The grey circled numbers label the multiples from the velocity contrast of interest. (b) is as (a) but with the sumodel to 12 km, in (c) the model is to 17 km, in (d) the model is to 56 km, highlighting the contribution from the velocity contrast around the Moho and (e) is the model to 72 km. It can be seen that the multiples from the velocity contrasts at 12 and 17 km (labelled 2 and 3 in grey circles) shown in (b) and (c) arrive at the same time as the conversion from the velocity contrast around 50–56 km shown in (d).

We have added significantly to previous previous fundamental mode group velocity dispersion measurements made for this area, in particular at short periods, helped particularly by the inclusion of dispersion curves obtained from the cross-correlation of ambient noise data. This has highlighted the value of making such measurements to provide tighter constraints on crustal shear velocities obtained from the inversion of group velocity data. Further improvements to the constraints on crustal shear velocity structure are also provided by the inclusion of receiver function data in the inversions. We are able to fit both the *P* receiver function data and group velocity data well with the same model. Including *S* receiver function data in the inversion appears to marginally improve the the rms misfit values to the *P* receiver function and surface wave data and improves the overall misfit. Including such observations in the joint analysis is useful, despite the fits to the SRF data being relatively poor and inclusion of the *S* receiver function data not altering the interpretation. Additionally, we find that joint inversion can help to evaluate the extent to which various features in the receiver functions are amplified or eliminated by interference from multiples, which greatly reduces the ambiguity in interpretation.

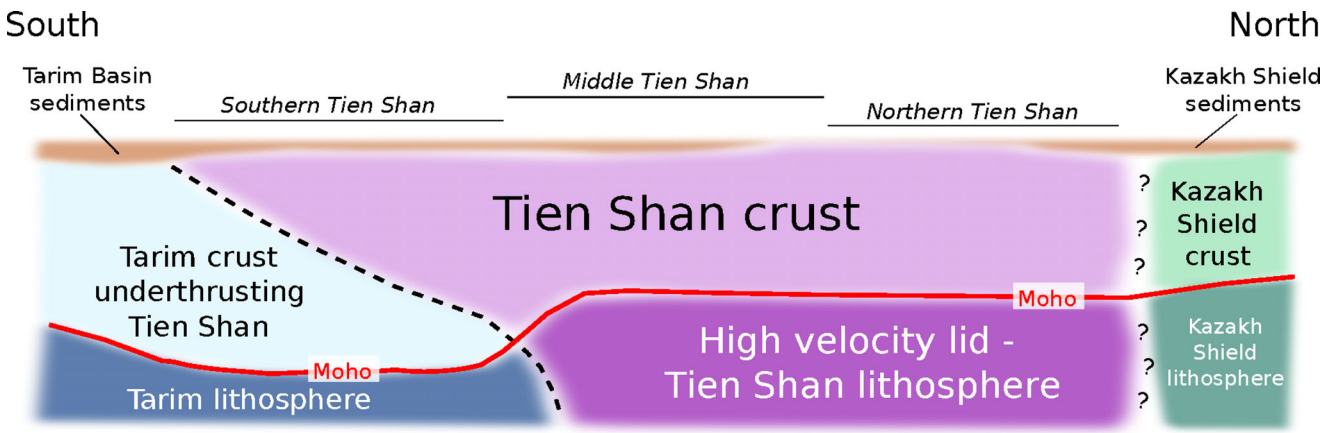

Figure 15. Cartoon summarizing the key interpretations of this study. The Tarim crust is understhrusting the Tien Shan from the south. The northward extent of the underthrusting of the the Tarim crust coincides with the boundary observed at the surface between the Southern and Central Tien Shan terranes. Underthrusting is responsible for thickened crust beneath the southern Tien Shan. A high velocity lid in the upper mantle is found beneath the central and northern Tien Shan. The depth of the Moho in this region does not vary significantly.

ACKNOWLEDGEMENTS

The collection and archiving of the data used in this study was supported by the IRIS PASSCAL and DMS programs and by the NSF Continental Dynamics Project EAR 0309927. Amy Gilligan is supported by a NERC studentship, with CASE funding from Weston Geophysical. Figures were prepared using Generic Mapping Tools (GMT) software (Wessel & Smith 1998). We thank two anonymous reviewers for their comments.

REFERENCES

Abdrakhmatov, K.Ye. *et al.*, 1996. Relatively recent construction of the Tien Shan inferred from GPS measurements of present-day crustal deformation rates, *Nature,* **384**(6608), 450–453.

Acton, C.E., Priestley, K., Gaur, V.K. & Rai, S.S., 2010. Group velocity tomography of the Indo-Eurasian collision zone, *J. geophys. Res.,* **115**(B12), B12335, doi:10.1029/2009JB007021.

Allen, M.B., Vincent, S.J. & Wheeler, P.J., 1999. Late Cenozoic tectonics of the Kepingtage thrust zone: interactions of the Tien Shan and Tarim Basin, northwest China, *Tectonics,* **18**(4), 639–654.

Ammon, C.J., 1991. The isolation of receiver effects from teleseismic P waveforms, *Bull. seism. Soc. Am.,* **81**(6), 2504–2510.

Avouac, J.P., Tapponnier, P., Bai, M., You, H. & Wang, G., 1993. Active thrusting and folding along the Northern Tien Shan and Late Cenozoic rotation of the Tarim relative to Dzungaria and Kazakhstan, *J. geophys. Res.,* **98**(B4), 6755–6804.

Beauchamp, W., Barazangi, M., Demnati, A. & El Alji, M., 1996. Intracontinental rifting and inversion: Missour basin and Atlas mountains, morocco, *AAPG Bull.,* **80**(9), 1459–1481.

Bensen, G.D., Ritzwoller, M.H., Barmin, M.P., Levshin, A.L., Lin, F., Moschetti, M.P., Shapiro, N.M. & Yang, Y., 2007. Processing seismic ambient noise data to obtain reliable broad-band surface wave dispersion measurements, *Geophys. J. Int.,* **169**(3), 1239–1260.

Bullen, M.E., Burbank, D.W. & Garver, J.I., 2003. Building the Northern Tien Shan: integrated thermal, structural, and topographic constraints, *J. Geol.,* **111**(2), 149–165.

Bump, H.A. & Sheehan, A.F., 1998. Crustal thickness variations across the northern Tien Shan from teleseismic receiver functions, *Geophys. Res. Lett.,* **25**(7), 1055–1058.

Burtman, V.S., 1975. Structural geology of Variscan Tien Shan, *Am. J. Sci.,* **275,** 157–186.

Chen, Y.H., Roecker, S.W. & Kosarev, G.L., 1997. Elevation of the 410 km discontinuity beneath the central Tien Shan: evidence for a detached lithospheric root, *Geophys. Res. Lett.,* **24**(12), 1531–1534.

English, J.M. & Johnston, S.T., 2004. The Laramide orogeny: what were the driving forces?, *Int. Geol. Rev.,* **46**(9), 833–838.

Farra, V. & Vinnik, L., 2000. Upper mantle stratification by P and S receiver functions, *Geophys. J. Int.,* **141**(3), 699–712.

Geuzaine, C. & Remacle, J.-F., 2009. Gmsh: a three-dimensional finite element mesh generator with built-in pre- and post-processing facilities, *Int. J. Numer. Methods. Eng.,* **79**(11), 62–626.

Gomberg, J.S. & Masters, T.G., 1988. Waveform modelling using locked-mode synthetic and differential seismograms: application to determination of the structure of Mexico, *Geophys. J.,* **94**(2), 193–218.

Haskell, N.A., 1960. Crustal reflection of plane SH waves, *J. geophys. Res.,* **65**(12), 4147–4150.

Haskell, N.A., 1962. Crustal reflection of plane P and SV waves, *J. geophys. Res.,* **67**(12), 4751–4768.

Herrmann, R.B. & Ammon, C.J., 2004. *Computer Programs in Seismology: Surface waves, Receiver Functions and Crustal Structure,* Saint Louis University.

Juli, J., Ammon, C.J., Herrmann, R.B. & Correig, A.M., 2000. Joint inversion of receiver function and surface wave dispersion observations, *Geophys. J. Int.,* **143**(1), 99–112.

Kennett, B.L.N. & Engdahl, E.R., 1991. Traveltimes for global earthquake location and phase identification, *Geophys. J. Int.,* **105**(2), 429–465.

Kennett, B.L.N., Engdahl, E.R. & Buland, R., 1995. Constraints on seismic velocities in the Earth from traveltimes, *Geophys. J. Int.,* **122**(1), 108–124.

Kind, R., Yuan, X. & Kumar, P., 2012. Seismic receiver functions and the lithosphere–asthenosphere boundary, *Tectonophysics,* **536,** 25–43.

Krestnikov, V.N., Nersesov, I.L. & Shfange, D.V., 1982. Quaternary tectonics and deep structure of the Pamir and Tien Shan, *Int. Geol. Rev.,* **24**(7), 745–758.

Langston, C.A., 1979. Structure under Mount Rainier, Washington, inferred from teleseismic body waves, *J. geophys. Res.,* **84**(B9), 4749–4762.

Laske, G. & Masters, G., 1997. A global digital map of sediment thickness, *EOS, Trans. Am. geophys. Un.,* **78,** F483.

Li, Z., Roecker, S., Li, Z., Wei, B., Wang, H., Schelochkov, G. & Bragin, V., 2009. Tomographic image of the crust and upper mantle beneath the western Tien Shan from the MANAS broadband deployment: possible evidence for lithospheric delamination, *Tectonophysics,* **477**(1-2), 49–57.

Makarov, V.I. *et al.*, 2010. Underthrusting of Tarim beneath the Tien Shan and deep structure of their junction zone: main results of seismic experiment along MANAS Profile Kashgar-Song-Kl, *Geotectonics,* **44**(2), 102–126.

Makeyeva, L.I., Vinnik, L.P. & Roecker, S.W., 1992. Shear-wave splitting and small-scale convection in the continental upper mantle, *Nature,* **358**(6382), 144–147.

Mitra, S., Priestley, K., Gaur, V.K., Rai, S.S. & Haines, J., 2006. Variation of Rayleigh wave group velocity dispersion and seismic heterogeneity of the Indian crust and uppermost mantle, *Geophys. J. Int.,* **164**(1), 88–98.

Molnar, P. & Ghose, S., 2000. Seismic moments of major earthquakes and the rate of shortening across the Tien Shan, *Geophys. Res. Lett.,* **27**(16), 2377–2380.

Molnar, P. & Tapponnier, P., 1975. Cenozoic tectonics of Asia: effects of a continental collision, *Science,* **189,** 419–426.

Ni, J., 1978. Contemporary tectonics in the Tien Shan region, *Earth planet. Sci. Lett.,* **41**(3), 347–354.

Nunn, C., Roecker, S.W., Priestley, K.F., Liang, X. & Gilligan, A., 2014. Joint inversion of surface waves and teleseismic body waves across the Tibetan collision zone: the fate of subducted indian lithosphere, *Geophys. J. Int.,* **198**(3), 1526–1542.

Oreshin, S., Vinnik, L., Peregoudov, D. & Roecker, S., 2002. Lithosphere and asthenosphere of the Tien Shan imaged by S receiver functions, *Geophys. Res. Lett.,* **29**(8), 32-1–32-4.

Özalaybey, S., Savage, M.K., Sheehan, A.F., Louie, J.N. & Brune, J.N., 1997. Shear-wave velocity structure in the northern Basin and Range province from the combined analysis of receiver functions and surface waves, *Bull. seism. Soc. Am.,* **87**(1), 183–199.

Poupinet, G. *et al.*, 2002. Intracontinental subduction and Palaeozoic inheritance of the lithosphere suggested by a teleseismic experiment across the Chinese Tien Shan, *Terra Nova,* **14**(1), 18–24.

Pratt, R.G., Song, Z.-M., Williamson, P. & Warner, M., 1996. Two-dimensional velocity models from wide-angle seismic data by wavefield inversion, *Geophys. J. Int.,* **124**(2), 323–340.

Reigber, Ch. *et al.*, 2001. New space geodetic constraints on the distribution of deformation in Central Asia, *Earth planet. Sci. Lett.,* **191**(1), 157–165.

Rham, D.J., 2009. The crustal structure of the Middle East, *PhD thesis,* University of Cambridge, UK.

Roecker, S., 2001. Constraints on the crust and upper mantle of the Kyrgyz Tien Shan from the preliminary analysis of GHENGIS broad-band seismic data, *Geologiya I Geofizika,* **42**(10), 1554–1565.

Roecker, S.W., Sabitova, T.M., Vinnik, L.P., Burmakov, Y.A., Golvanov, M.I., Mamatkanova, R. & Munirova, L., 1993. Three-dimensional elastic wave velocity structure of the western and central Tien Shan, *J. geophys. Res.,* **98**(B9), 15 779–15 795.

Roecker, S., Thurber, C. & McPhee, D.,, 2004. Joint inversion of gravity and arrival time data from Parkfield: new constraints on structure and hypocenter locations near the SAFOD drill site, *Geophys. Res. Lett.,* **31**(12), doi:10.1029/2003GL019396.

Searle, M.P. *et al.*, 1987. The closing of Tethys and the tectonics of the Himalaya, *Geol. Soc. Am. Bull.,* **98**(6), 678–701.

Shapiro, N.M. & Campillo, M., 2004. Emergence of broadband Rayleigh waves from correlations of the ambient seismic noise, *Geophys. Res. Lett.,* **31**(7), doi:10.1029/2004GL019491.

Silva, W., 1976. Body waves in a layered anelastic solid, *Bull. seism. Soc. Am.,* **66**(5), 1539–1554.

Sloan, R.A., Jackson, J.A., McKenzie, D. & Priestley, K., 2011. Earthquake depth distributions in central Asia, and their relations with lithosphere thickness, shortening and extension, *Geophys. J. Int.,* **185**(1), 1–29.

Sobel, E.R. & Dumitru, T.A., 1997. Thrusting and exhumation around the margins of the western Tarim basin during the India-Asia collision, *J. geophys. Res.,* **102**(B3), 5043–5063.

Tapponnier, P. & Molnar, P., 1979. Active faulting and Cenozoic tectonics of the Tien Shan, Mongolia, and Baykal regions, *J. geophys. Res.: Solid Earth (1978–2012),* **84**(B7), 3425–3459.

Thompson, S.C., Weldon, R.J., Rubin, C.M., Abdrakhmatov, K., Molnar, P. & Berger, G.W., 2002. Late Quaternary slip rates across the central Tien Shan, Kyrgyzstan, central Asia, *J. geophys. Res.,* **107**(B9), ETG 7-1–ETG 7-32.

Vinnik, L., 1977. Detection of waves converted from P to SV in the mantle, *Phys. Earth planet. Inter.,* **15**(1), 39–45.

Vinnik, L.P. & Saipbekova, A.M., 1984. Structure of the lithosphere and the asthenosphere of the Tien Shan, *Ann. Geophys.,* **2**(6), 621–626.

Vinnik, L.P., Reigber, C., Aleshin, I.M., Kosarev, G.L., Kaban, M.K., Oreshin, S.I. & Roecker, S.W., 2004. Receiver function tomography of the central Tien Shan, *Earth planet. Sci. Lett.,* **225**(1–2), 131–146.

Vinnik, L., Aleshin, I., Kaban, M., Kiselev, S., Kosarev, G., Oreshin, S. & Reigber, Ch., 2006. Crust and mantle of the Tien Shan from data of the receiver function tomography, *Izvest Phys. Solid Earth,* **42**(8), 639–651.

Wang, Q. *et al.*, 2001. Present-day crustal deformation in China constrained by global positioning system measurements, *Science,* **294**(5542), 574–577.

Wessel, P. & Smith, W.H.F., 1998. New improved version of generic mapping tools released, *EOS, Trans. Am. geophys. Un.,* **79**(47), 579, doi:10.1029/98EO00426.

Windley, B.F., Allen, M.B., Zhang, C., Zhao, Z.-Y. & Wang, G.-R., 1990. Paleozoic accretion and Cenozoic redeformation of the Chinese Tien Shan Range, central Asia, *Geology,* **18**(2), 128–131.

Yin, A., Nie, S., Craig, P., Harrison, T.M., Ryerson, F.J., Xianglin, Q. & Geng, Y., 1998. Late cenozoic tectonic evolution of the southern Chinese Tian Shan, *Tectonics,* **17**(1), 1–27.

Zubovich, A.V. *et al.*, 2010. GPS velocity field for the Tien Shan and surrounding regions, *Tectonics,* **29**(6), doi:10.1029/2010TC002772.

SUPPORTING INFORMATION

Additional Supporting Information may be found in the online version of this article:

Figure S1. Test for robustness of features in the velocity model for bin 110. The brown line shows the resultant group velocities for bin 110 for a model with the low velocity zone between 37 km and 80 km removed.

Figure S2. As Figure S1 but for bin 270, with the high velocity zone between 57 km and 120 km set to the same velocity as at 57 km.

Figure S3. Tests for the contribution of velocity contrasts in the model (left) to the synthetic P receiver function (right) for bin 110.

Figure S4. Test showing the fit of the synthetic P receiver function calculated for the velocity model from the inversion of just surface wave data for bin 110.

Figure S5. As Figure S4 but for bin 270 (http://gji.oxfordjournals.org/lookup/suppl/doi:10.1093/gji/ggu225/-/DC1).

Please note: Oxford University Press are not responsible for the content or functionality of any supporting materials supplied by the authors. Any queries (other than missing material) should be directed to the corresponding author for the article.